

Computational study of the shock driven instability of a multi-phase particle-gas system

J. A. McFarland, W. J. Black, J. Dahal, B. E. Morgan

August 24, 2015

Physics of Fluids

Disclaimer

This document was prepared as an account of work sponsored by an agency of the United States government. Neither the United States government nor Lawrence Livermore National Security, LLC, nor any of their employees makes any warranty, expressed or implied, or assumes any legal liability or responsibility for the accuracy, completeness, or usefulness of any information, apparatus, product, or process disclosed, or represents that its use would not infringe privately owned rights. Reference herein to any specific commercial product, process, or service by trade name, trademark, manufacturer, or otherwise does not necessarily constitute or imply its endorsement, recommendation, or favoring by the United States government or Lawrence Livermore National Security, LLC. The views and opinions of authors expressed herein do not necessarily state or reflect those of the United States government or Lawrence Livermore National Security, LLC, and shall not be used for advertising or product endorsement purposes.

Computational study of the shock driven instability of a multiphase particle-gas system

Jacob A. McFarland,^{1, a)} Wolfgang J. Black,¹ Jeevan Dahal,¹ and Brandon E. Morgan²

1) University of Missouri Department of Mechanical and Aerospace Engineering,
E2412 Lafferre Hall, Columbia, MO 65211

²⁾Lawrence Livermore National Laboratory, 7000 East Ave. PO Box 808, L-170 Livermore, CA 94550

(Dated: January 11, 2016)

This paper considers the interaction of a shock wave with a multiphase particle-gas system which creates an instability similar in some ways to the Richtmyer-Meshkov instability but with a larger parameter space. As this parameter space is large, we only present an introductory survey of the effects of many of these parameters. We highlight the effects of particle-gas coupling, incident shock strength, particle size, effective system density differences, and multiple particle relaxation time effects. We focus on dilute flows with mass loading up to 40% and do not attempt to cover all parametric combinations. Instead, we vary one parameter at a time leaving additional parametric combinations for future work. The simulations are run with the Ares code, developed at Lawrence Livermore National Laboratory, which uses a multiphase particulate transport method to model two-way momentum and energy coupling. A brief validation of these models is presented and coupling effects are explored. It is shown that even for small particles, on the order of $1\mu m$, multi-phase coupling effects are important and diminish the circulation deposition on the interface by up to 25%. These coupling effects are shown to create large temperature deviations from the dusty gas approximation, up to 20% greater, especially at higher shock strengths. It is also found that for a multiphase instability, the vortex sheet deposited at the interface separates into two sheets. Depending on the particle and particle-gas Atwood numbers, the instability may be suppressed or enhanced by the interactions of these two vortex sheets.

PACS numbers: 47.40.Nm 47.20.Ma 47.55.Kf

Keywords: Multiphase flow, Richtmyer-Meshkov instability, Fluid Instability

a) mcfarlandja@missouri.edu

I. INTRODUCTION

The purpose of this paper will be to explore the effects of shock driven hydrodynamic instabilities in particle-gas systems. This complex system has been seldom studied on its own and involves a wide range of physics. While few works have addressed this system exactly, some previous works have covered aspects of it. To provide some background on this system, a brief review of some of the related works will be presented in this section first. We note, however, that there is a very broad range of related research, and it is not possible to cover all related works. We instead have provided a sample of some of these related works which will help give the reader an idea of where our research fits in among the previous literature.

The shock driven multi-phase instability is closely related to the Richtmyer-Meshkov (RM) instability^{1,2} in the case of small, fast reacting particles (as seen in section IV C). This instability is created by the impulsive acceleration of an interface between two fluids of different densities. This interaction results in the deposition of baroclinic vorticity, seen in equation 1, created by the misalignment of the pressure and density gradients. In equation 1, $\frac{D\overrightarrow{\omega}}{Dt}$, $\overrightarrow{\omega}$, u, ν , ρ , and P are the material derivative of vorticity, vorticity, velocity vector, kinematic viscosity, density, and pressure, respectively. From the baroclinic term, it can be seen that three ingredients are necessary for the RM instability: a density gradient, a pressure gradient, and a misalignment between the two.

$$\frac{D\overrightarrow{\omega}}{Dt} = \overrightarrow{\omega} \cdot \overrightarrow{\nabla} \overrightarrow{u} + \nu \nabla^2 \overrightarrow{\omega} + \left[\frac{1}{\rho^2} \overrightarrow{\nabla} \rho \times \overrightarrow{\nabla} P\right]_{baroclinic\ term} \tag{1}$$

The RM instability appears in inertial confinement fusion where its occurrence drives mixing between layers of the fuel capsule resulting in degraded performance³. In astrophysics, the RM instability appears in supernovae (SNe) events, driven by blast waves, where it drives mixing along with the Rayleigh-Taylor instability^{4,5}. In SNe, RM instability driven ejecta spikes can drive material from the star core out into the interstellar medium (ISM). Cosmic dust can be produced in these ejecta⁶. The production and survival of dust from SNe is an important possible source for cosmic dust which is still debated⁷. Dust mass fractions, typically described by the overdensity ratio, are high, approximately 99% or greater, while the volume fractions are low, approaching zero due to the low gas densities⁸. Shock driven hydrodynamics may also play an important role in dust production from asymptotic

giant branch stars^{9,10}. In these events, shock driven hydrodynamics play an important role in mass distribution and nucleation of solid particles⁸.

Shock driven multi-phase flows often arise in RM research as particles are used as passive tracers for the gas phase. Balakumar $et~al.^{11}$ used particle imaging velocimetry (PIV) with fog particles along with laser induced fluorescence of acetone vapor to get simultaneous velocity and density measurements in a reshocked turbulent RM flow. Jacobs $et~al.^{12}$ used incense smoke to mark one species and then used Mie scattering of laser light from the particles to track the gas location during RM instability experiments. Haehn $et~al.^{13}$ used liquid particles up to $25\mu m$ in diameter created by the destruction of a soap film membrane to get PIV measurements of the velocity field in a shock bubble interaction. McFarland $et~al.^{14}$ used sub-micron diameter glycerol particles to track gasses using the Mie scattering technique in inclined interface RM experiments. Recent work from Reilly $et~al.^{15}$ presented a 2D field of uncertainty in velocities calculated using PIV measurements with sub-micron glycerol particles.

Most of these studies have not closely addressed issues related to the ability of the particles to track the flow. As the particles lag behind the gases, they reduce the accuracy of measurements made using them. At large enough concentrations, the particles could effect the evolution of the RM instability, adding shock-multiphase effects. The ability of particles to track the flow behind high strength blast waves was addressed in experiments by Murphy and Adrian¹⁶. In these experiments, it was found that $1\mu m$ olive oil particles had too long of a relaxation time to accurately follow the flow behind blast waves with Mach numbers up to 2.17. Various experimental works^{17,18} have examined the acceleration of particles behind shock waves to determine drag coefficients. Recent work from Martinez et al. 19 studied the acceleration of various particles behind a shock wave and found drag coefficients that differ from previous models based on other shock-particle regimes. Theoretical works^{20,21} have also examined the drag forces on a particle resulting from a shock interaction and found good agreement with some experiments. The interaction of a shock wave with a dense particle field not only perturbs the gas but can create a complex system of shock refraction. Wagner et al.²² performed experiments with a cloud sheet of $100\mu m$ glass particles and shock waves up to Mach 1.95 which showed increased peak post shock pressures in the cloud interface vicinity.

The work of Vorobieff et al.²³ explored the effect of particles in RM instabilities and first

identified that an instability could be created by a shock interaction with a multi-phase system interface alone. In this paper, the authors showed that a cloud of sub-micron particles could induce an instability and mixing similar to a RM instability. Further work²⁴ investigated the role of particles in a shock-cylinder RM instability with experiments and simulations. Their work showed good qualitative agreement between particle-in-cell simulations and experiments.

In a multiphase particle system, the continuous phase is referred to as the carrier phase or carrier gas, and the particles are referred to as the dispersed phase. The ratio of particle to carrier gas mass is known as the particle mass loading ϕ_m while the ratio of volumes is referred to as the particle volume fraction ϕ_{vp} . At small ϕ_m and ϕ_{vp} , the particle effects can be ignored²⁵. As the particle concentration increases, though, their effect becomes significant, and momentum, energy, and mass transfer between the phases becomes important. Marble²⁶ produced an early review of multi-phase systems of solid or liquid particles suspended in a gas referred to as a dusty gas. In this previous work, various particle relaxation times based on momentum exchange, heat transfer, and phase change are defined using simplifications to the problem. If these relaxation times are small compared to the characteristic time of the flow, then equilibrium can be assumed between the gas and particles. With this assumption, the dusty gas model can be used where the particle-gas system is modeled as a single gas with averaged properties. This approach is powerful in that it allows for a single equation of state to be used and greatly reduces the number of equations needed to model the flow. $Saffman^{27}$ found in theoretical work that for laminar flows of dusty fluids, the relaxation times of the particles effected the stability of the flow. He found that for large particles with long relaxation times, the flow was stabilized compared to a flow with small particles and short relaxation times.

Various computational approaches have been developed to explore multi-phase particle-gas systems. The particle-in-cell (PIC) method superimposes a Lagrangian coordinate system over the Eulerian one, combining the best of particle and fluid methods²⁸. Andrews and O'Rourke²⁹ modified the PIC method to develop a closely coupled multiphase particle in cell (MP-PIC) method with an ability to handle dilute to dense particle loadings with a wide range of sizes and distributions. In this model, the particle is represented both as a discrete phase and in the continuum. This representation helps utilize the best of both of Eulerian-Eulerian continuum models and Eulerian-Lagrangian discrete models. Snider et

al.³⁰ improved this method with an improved grid-to-particle interpolation method, extending it to three dimensions with a fully implicit particle and fluid phase couplings giving a robust solution. Patanker and Joseph³¹ developed a Lagrangian numerical simulation (LNS) scheme by extending the MP-PIC model to incorporate the viscous effects of the fluid phase. The MP-PIC model is in fact the extension of the KIVA code, which uses the stochastic particle method in which the isotropic particle stress gradient has been added to the equation of motion of the particle³². This addition enables the code to handle dense particulate flows without reaching the closed pack limits. The stochastic particle method has an additional turbulent particle velocity component u_{tp} that models the random unresolved particle velocity (we do not use this term in our simulations). Due to the absence of the particle continuum equation, the stochastic particle method does not have the advantage of implicitly coupling the advanced time void fraction to the conservation equation and is limited to using the previous time step or auxiliary void fraction of the particle. The solution is obtained in three steps: 1) the particle properties are interpolated to the grid points, 2) the source terms for the mass, momentum and energy are calculated and used to calculate the advanced time fluid properties, and 3) these properties are then interpolated to calculate new time particle properties.

Various studies have been done to find the best model for the drag coefficient in the shock tube environment. The simplest is the Stokes' drag model, which gives a good approximation of the inverse variation of the drag coefficient with the Reynolds number(Re) in the Stokes flow Regime, i.e Re < 1. A good fit for the standard drag curve beyond the Stokes flow regime is given by the Kliachko model^{33,34} which represents the standard drag coefficient to better than 5% for Re up to about 500 and better than 10% for Re up to 1000^{35} . At higher Reynolds number, the Drag coefficient can be approximated by a constant value of 0.425 up to a critical Reynolds number³⁶. These results were generalized by O' Rourke and Brocca³⁷ for the dependence of drag coefficient, C_D , on the gas volume fraction, ϕ_{vg} , and were later verified by the experiments of Richardson and Zaki³⁸. Rudinger's experiments showed a large deviation in the actual drag coefficient in the shock tube to the Kliachko drag for Re up to 300^{39} . In addition, it showed that the Rudinger correlation provides better approximation in this range. Steady force effects like compressibility and rarefaction, particle cloud pressure gradient and buoyant force, and unsteady force effects like virtual and apparent mass (Basset force) and turbulence effects modify the drag coefficient³⁶. Drag

models formulated by various authors considering these effects have been given by Crowe et al.³⁶.

The paper will be organized as follows: first, we will detail the computational methods of our simulations. Next, we will examine the differences between particle driven instabilities and the RM instability, and then we will explore the effects of incident shock strength, particle size and relaxation time, particle-gas system Atwood numbers. Finally, we will conclude with a brief study of a two particle relaxation time driven instability.

II. PARTICLE-GAS SYSTEM HYDRODYNAMIC PARAMETERS

This section provides a set of definitions for terms to describe the particle-gas system hydrodynamics. We start with the adaptation of parameters defined for the related RM instability. The density difference for an RM or Rayleigh-Taylor instability is characterized by the gas Atwood number defined in equation 2 where the subscripts 1 and 2 indicate the upstream and downstream gases, respectively. The Mach number characterizes the pressure gradient or acceleration strength and is defined in equation 3 where w_i is the incident shock wave speed and c_g is the gas sound speed. For the particle-gas system, we define a particle-gas Atwood number (eq. 4) where ρ_{pg} is the combined particle-gas system density. The presence of particles modifies the effective sound speed of the particle-gas system as well, but we limit ourselves in this paper to defining the acceleration strength based on the Mach number of an incident shock in a pure gas.

$$A_g = \frac{\rho_{g2} - \rho_{g1}}{\rho_{g1} + \rho_{g2}} \tag{2}$$

$$M = \frac{w_i}{c_g} \tag{3}$$

$$A_{pg} = \frac{\rho_{pg2} - \rho_{pg1}}{\rho_{pg1} + \rho_{pg2}} \tag{4}$$

To describe the particles and their ability to equilibriate with the carrier gas, we need to define a particle Stokes number. The Stokes number is qualitatively defined as the ratio of a characteristic time of the particle to a characteristic time of the fluid, $St = \frac{\tau_p}{\tau_g}$. Low Stokes numbers indicate the particles respond fast to changes in the fluid flow. To define the

Stokes number in a hydrodynamic flow, we adapt a method for particles in a fully turbulent flow²⁵. The particle characteristic time is defined as in equation 5, where d is the particle diameter, ρ_p is the particle density, and Re is the flow Reynolds number (eq. 7). The gas characteristic time (eq. 6) is found as a modified Kolmogorov time constant, where the characteristic length scale is chosen to be the interface wavelength λ , and the characteristic velocity is chosen to be the interface jump velocity for the particle-gas system $[u_{pg}]$ found using one dimensional gas dynamics calculations. The flow Reynolds number is found using a definition similar to RM instability work in equation 7, where $\dot{h_0}$ is the interface growth rate, and we use the average initial viscosity of the interface gases. In order to determine the particle Stokes number a priori we use the interface initial wavelength as the length scale instead of the instantaneous interface height and the initial linear growth rate predicted by the Richtmyer impulsive model. The Richtmyer impulsive model is given in equation 8, where A'_{pg} is the post shock Atwood number for the particle-gas system, and η' is the post shock amplitude predicted by equation 9 with η_0 being the initial interface amplitude.

$$\tau_p = \frac{d^2 \rho_p / \rho_g}{18\nu (1 + 0.15Re^{0.687})} \tag{5}$$

$$\tau_g = \left(\frac{\nu\lambda}{[u_{pg}]}\right)^{0.5} \tag{6}$$

$$Re = \frac{\lambda |\dot{h_0}|}{(\nu_1 + \nu_2)/2} \tag{7}$$

$$\dot{h_0} = \frac{2\pi/\lambda}{[u_{pg}]A'_{pg}\eta'} \tag{8}$$

$$\eta' = \eta_0 \left(1 - \frac{[upg]}{w_i} \right) \tag{9}$$

Following the methods of Marble²⁶, we define characteristic times for thermal and velocity relaxation. The velocity relaxation time is defined in equation 10, where μ is the gas dynamic viscosity, and m_p is the mass of a single particle defined as $m_p = 4/3\pi \rho_p r^3$. The thermal relaxation time is defined in equation 12, where C_p is the specific heat of the particle material, and κ is the thermal conductivity of the carrier gas. For most gases, the properties will be such that $\tau_V \approx \tau_T$, and we will refer to them together by $\tau_{V/T}$. We take the characteristic

time of the interface hydrodynamics to be the shock transit time, $t_c = \eta_0/w_i$. The ratio of the characteristic relaxation to hydrodynamic times, $\tau_V = t_V/t_c$ and $\tau_T = t_T/t_c$, gives us an estimate of the importance of particle-gas momentum and energy coupling. We will take $\tau_V \ll 0.1$ and $\tau_T \ll 0.1$ to mean the particle coupling effects are negligible. In this case, the dusty gas approximation will yield similar results (sect. VI). The dusty gas approximation treats the particle-gas system as a continuous gas with the average properties of the particle and carrier gas. The particle-gas system is approximated as a single gas with an equivalent gas constant (eq. 13) and ratio of specific heats (eq. 14). Table I provides a summary of the particle parameters presented in this section for reference in later sections.

$$t_V = \frac{m_p}{6\pi (d/2)^2 \mu} \tag{10}$$

$$m_p = 4/3\pi\rho_p r^3 \tag{11}$$

$$t_T = \frac{m_p C_p}{4\pi (d/2)^2 \kappa} \tag{12}$$

$$R_{pg} = \frac{P}{(\rho_g \phi_{vp} + \rho_p (1 - \phi_{vp}))T}$$
 (13)

$$\gamma_{pg} = \frac{\phi_{vp}\rho_g C_{Pg} + (1 - \phi_{vp})\rho_p C_p}{\phi_{vp}\rho_g C_{Vg} + (1 - \phi_{vp})\rho_p C_p}$$
(14)

III. COMPUTATIONAL CODE

A. Ares code

The computational study was performed using the Ares code, a staggered mesh arbitrary Lagrange Eulerian (ALE) hydrodynamics code developed at Lawrence Livermore National Laboratory. The Lagrange time advancement is second-order predictor-corrector and uses the Gauss Divergence theorem to give the discrete finite difference equations⁴⁰. All numerical differences are fully second order in space. Velocities are defined at mesh nodes, and density and internal energy are defined at the zone centers using piece-wise constant profiles. Artificial viscosity is used to suppress spurious oscillations⁴¹. A second-order remap⁴²

Table I. Particle parameters reference table

| Symbol | description |
|----------|----------------------------|
| A_g | Atwood number based on the |
| | gas densities |
| A_{pg} | Atwood number based on the |
| | combined gas and particle |
| | densities |
| St | Particle Stokes number |
| $	au_V$ | Nondimensional velocity |
| | relaxation time |
| $	au_t$ | Nondimensional thermal |
| | relaxation time |
| | |

is applied to the solution after the Lagrange step. In these simulations, a fixed Eulerian mesh is used at all times. The Ares code includes an adaptive mesh refinement (AMR) capability that allows the base resolution to be increased by a factor of three for each level of refinement. The refinement is performed on areas that exceed an error tolerance in the computation of a second undivided difference of pressure and on all mixed zones. The AMR approach implemented in Ares follows that of Berger and Oliger⁴³ and Berger and Colella⁴⁴. Time advancement is not recursive though, and the coarser levels are slaved to run at the finest level time step. This approach has been extensively studied and provides a factor of 5 to 7 increase in efficiency over a fully refined everywhere simulation. In the current AMR implementation, the particles must reside in fully refined regions while the carrier gas only regions may exist at the lowest level of refinement. Allowing the carrier gas only regions to exist at low levels of refinement allows us to accurately model larger problems with shock boundary interactions, such as reshock, with only a modest increase in computational time.

The Ares code solves the Navier-Stokes equations for multi-species flows, conservation of mass, momentum, and energy. A summary of these equations can be found in previous work⁴⁵. In addition to these equations, Ares uses a particle package that employs a multi-phase particle transport method to couple particles calculated on a Lagrangian point mesh

to the continuous carrier phase on an Eulerian mesh. The Ares particle package is fully functional with the AMR capabilities employed on the Eulerian mesh and can be used for 2D or 3D problems. We adopt the notation of the previous work in the following section to show the modified equations for the particle package. These equations are given in Einstein notation where the super/subscripts i, j, and k denote direction indices, and m and n denote species indices. Summation is implied between superscripts and subscripts with repeated indices and Hadamard products (element-wise product) are implied by repeated superscripts or repeated subscripts. The computational particles on the point mesh represent packets of physical particles. The computational particles carry and update variables for particle size, velocity, and temperature. The particles are assumed to be spherical and incompressible. The particle package modifies the equations for conservation of mass, momentum, and energy in the carrier phase to allow particle-gas coupling. The continuity equation is modified by the inclusion of the gas volume fraction ϕ_{vg} , which is $1-\phi_{vp}$, shown in equation 15, where Y_n is the mass fraction of species n, u^i is the fluid velocity, and φ_n^i is the mass flux of species n. The momentum equation is modified by the inclusion of a particle drag term shown in equation 16, where f_j is the momentum source from the particles, and T_i^i is the stress tensor. The energy equation is modified by the inclusion of energy source terms for heat transfer from the particle phase and drag heating as show in equation 17, where e is the specific internal energy, P is the pressure, κ_n is the thermal conductivity of species n, T_g is the fluid temperature, h_n is the specific enthalpy of species n, and Q_s is the particle heating source term. Drag heating effects are manifested through changes in the gas volume fraction, ϕ_{vg} , which appears in many terms. Additional information on the Ares code numerical methods can be found in previous work 46,47 .

$$\partial_t(\rho_g \phi_{vg} Y_n) + \partial_i(\phi_{vg} \rho_g Y_n u^i + \varphi_n^i) = 0 \tag{15}$$

$$\partial_t(\rho_q \phi_{vq} u_i) + \partial_i(\phi_{vq} \rho_q u^i u_i - T_i^i) + f_i = 0 \tag{16}$$

$$\partial_t(\phi_{vg}\rho_g e) + \partial_i(\phi_{vg}\rho_g e u^i) + P(\partial_i(\phi_{vg}u^i) + \partial_t\phi_{vg}) -\partial_i(\phi_{vg}\kappa_n\partial^i T_g - h_n\varphi_n^i) - \phi_{vg}T_j^i\partial_i u^j + Q_s = 0$$

$$(17)$$

The momentum equation for the particles is shown in equation 18, where r is the particle radius, and v_i is the particle velocity. The energy equation for the particles in shown in equation 19. The source term for the momentum equation, f_i , is found using the standard drag model (eq. 20) with the drag coefficient given by the Kliachko model^{33,34} shown in equation 21. The particle Reynolds number is given as $Re_p = 2\rho_g r |u_i - v_i|/\mu$, where the gas dynamic viscosity, μ , is approximated by the Sutherland law described in the previous work⁴⁵. The Kliachko model was developed for a single smooth, non-rotating particle at constant speed without turbulence and at low Mach numbers. While the particles in the work are subjected to gas flows that are below approximately Mach 0.5, they are subjected to a sudden jump in gas velocity by the shock wave. For this reason, the particle drag is likely not correct at early times, but this should have little effect on the late time hydrodynamics of the particle-gas system. The source term for the energy equation Q_s is found using the Ranz-Marshall correlation 48 and is shown in equation 22, where Pr is the fluid Prandtl number. The Ranz-Marshall correlation is valid for spherical non-evaporating particles. Particle evaporation, break-up, and agglomeration are not considered in the models used by the Ares code.

$$m_p \partial_t v_i + \frac{m_p}{\rho_p} \partial_i P + f_i = 0 \tag{18}$$

$$m_p C_p \partial_t T_p - Q_s = 0 (19)$$

$$f_i = \frac{3\rho_g C_D m_p}{8\rho_p r} |u_i - v_i| (u_i - v_i)$$
(20)

$$C_D(Re_p, \phi_{vg}) = 0.024\phi_{vg}^{-2.55} + 0.4\phi_{vg}^{-1.78}$$
if $Re_p > 1000$

$$= \frac{24}{Re_p\phi_{vg}^{2.65}} + \frac{4}{Re_p^{1/3}\phi_{vg}^{1.78}}$$
if $Re_p \le 1000$

$$(21)$$

$$Q_s = 4\pi r^2 \kappa (\phi_{vg}^{-1.75} + 0.3\phi_{vg}^{-1/2} Re_p^{1/2} Pr^{1/3}) (T_g - T_p)/r$$
(22)

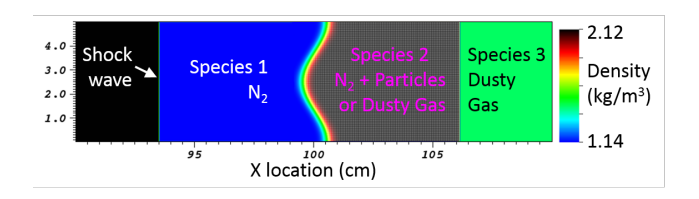


Figure 1. Typical initial conditions for the simulations

B. Initial conditions

For this work, we limited ourselves to a two dimensional study. The initial conditions for this work were chosen to be similar to common conditions used in previous works done on RM instability. The interface perturbation was chosen to be a simple sine wave perturbation with a wavelength of 5 cm ($\lambda = 5cm$) and an amplitude of 0.5 cm ($\eta = 0.5cm$). We define a linear interface to be one that has an amplitude to wavelength ration (η/λ) of less than 0.1, as has been done in previous works, and note that our perturbation is marginally linear ($\eta/\lambda = 0.1$). Three species, denoted S1, S2, and S3, are used in the simulation and create various interfaces. We use a 2D simulation for this work, as previous RM work⁴⁵ has shown that for a single dominant mode perturbation, 3D effects are limited before reshock, which is a second shock acceleration, even for high amplitude to wavelength ratio perturbations. For this work, our interface perturbation has a much lower amplitude to wavelength ratio than this previous work, and so we expect 3D effects to be negligible.

We limited the computational domain to one wavelength in height (y direction), while the width (x direction) was 250cm. We chose the width to allow for a sufficiently large development time from the incident shock interaction which was free of shock reflections from the upstream (x = 0cm) or downstream (x = 250cm) boundaries. The interface was initialized as seen in figure 1, centered an X location of 100 cm. The boundary conditions were no penetration, shock reflecting, and allowed slip. The upstream boundary contained a source term which supplied mass at the post shock conditions to sustain the shock wave. The interface was set up with a diffusion layer of 0.5 cm which was similar to previous experiments on a similar interface perturbation⁴⁹. The diffusion profile followed an error function as seen in previous experimental work¹⁴. The initial temperature and pressure were set to 300 K and 101.3 kPa, respectively.

The interface was set up numerically as two species for convenience (S1 and S2), although

in many simulations presented here, the species were identical in properties. Computational particles were initialized at all zone centers in S2 with a constant initial velocity of 0 and a constant radius which varies by simulation. Particles were modeled as ethylene glycol with a constant density of $1110kg/m^3$ and a specific heat of 2.84 kJ/kg-K. Each computational particle represented a number of physical particles where the number was set by a prescribed gas and particle-gas Atwood number (described in section II), which varied by simulation with typical numbers in the range of 100-20,000. In our simulation, the mass loading and volume fraction are driven by the parameters of A_g and A_{pg} . The mass loading varied by case from 12 to 40% and the volume fraction from 0.014 to 0.036%, which would make them dilute flows in multiphase flow terms.

The computational time required for a simulation scales with the number of computational particles, and so it was desirable to only include the minimum number of particles required to accurately model the interface interaction. To minimize the number of particles, the region of gas that contained particles (S2) was limited in the X direction downstream of the interface. This created a second effective interface between the particle containing gas (S2) and the downstream hydrodynamically inactive gas (S3) (fig. 1). To minimize the effect of shock deposited baroclinic vorticity at this interface, the properties of S3 were selected to match the average properties of the particle-gas system in S2. S3 essentially became a dusty gas approximation of the S2 particle-gas system. The interface between S2 and S3 was placed far enough downstream of the hydrodynamic interface that they were decoupled, and the transmitted shock had become planar again before passing through the second interface. The properties selected for S3 and the location of the S2-S3 interface resulted in no detectable shock reflection or hydrodynamic growth of this interface.

For ease of comparison, we define an exemplar case that will be used throughout the paper for comparison. The gas species were selected to be identical, nitrogen for both S1 and S2, so that the evolving instability could only be attributed to the presence of particles. The particle mass loading, ϕ_m , was set to 25% and the incident shock wave Mach number set to 1.5. The particle diameter was selected to be 2 μm , as it was near the upper limit of the estimated particle diameters in the previous experimental work of Anderson et al.²⁴ and produces marginally significant particle lag effects. These conditions yielded a particle Stokes number of approximately 0.2, with $\tau_v \approx \tau_T \approx 0.12$, and gas and particle-gas Atwood numbers of 0 and 0.11, respectively.

C. Resolution study

Before examining the results of the simulations presented in this work, it is necessary to estimate the errors due to the limitations of the resolution. For this purpose, we present the results of three simulations of the exemplar case with different levels of refinement. The maximum resolutions used for the study were $556\mu m$, $185\mu m$, and $62\mu m$, or 90, 270, and 810 nodes per perturbation wavelength. The simulation time (eq. 23) was non-dimensionalized by the characteristic time of the incident shock interface transit time described in section II. The species and particle fields are shown in figure 2 at a late time, $\tau = 200$, just prior to reshock. From this figure, it can be seen that the lowest resolution case evolves in a significantly different manner with diminished vortices, and a faster interface velocity, evident from the further downstream location of the interface. The major difference between the two high resolution cases is the development of secondary vorticity in the counter rotating vortices. This secondary vorticity deposition was shown to develop due to the acceleration created in the primary vortices⁵⁰.

$$\tau = t/t_c \tag{23}$$

Figures 3, 4, and 5 show the mixing width, circulation, and mixed mass for the three resolution cases over time. The mixing width, measured as the distance between the 5% and 95% contours of S1 or S2, shows little deviation between the three resolutions, but the low resolution case deviates at late times while the higher resolution cases remain similar. The positive circulation, defined in equation 24 where A is area and ω_+ is the positive component of vorticity, shows that the low resolution case overshoots initially and then dissipates faster. The two higher resolution cases are very similar at early times, but the highest resolution case shows an approximately 8% increase over the medium resolution case at late times due to the secondary vorticity deposition in the primary vortices. The S2 mixed mass is defined as the amount of S2 mass beyond the 50% contour of S1 (equations 25 and 26, where S_1 and S_2 subscripts refer to S1 and S2). This definition was used instead of more common definitions as it provides an analog to the particle mixed mass shown later in section VI. The S2 mixed mass again shows that the low resolution case is the outlier, while the highest resolution case is within approximately 5% of the medium resolution case. As resolution is increased further, we would expect to see diminishing changes in circulation and mixed

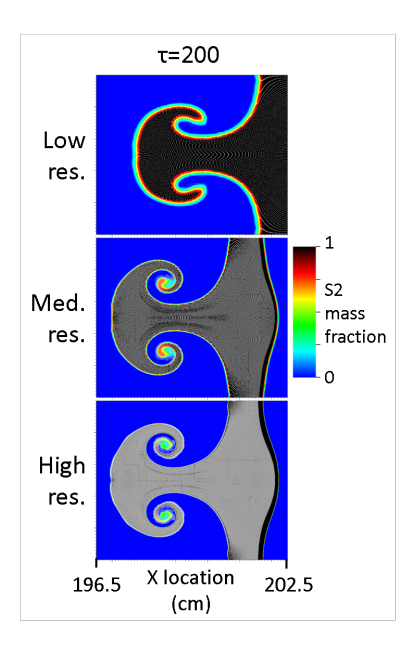


Figure 2. S2 mass fraction and particle locations for simulations at $\tau = 200$. Top: Low resolution 90 nodes per wavelength. Middle: Medium resolution 270 nodes per wavelength. Bottom: High resolution 810 nodes per wavelength.

mass. Since the medium resolution case is within 8% or less of the high resolution case, we use this resolution for the rest of the simulations presented, acknowledging that we are losing some amount of circulation and mixing due to this resolution limitation.

$$\Gamma_{+} = \int \omega_{+} dA \tag{24}$$

$$m_{S_2} = \frac{1}{A} \int Y_{S_2 S_1} \rho_g dA \tag{25}$$

$$Y_{S_2S_1} = Y_{S_2} \text{ if } Y_{S_1} \ge 0.5$$

= 0 if $Y_{S_1} < 0.5$ (26)

D. Validation versus analytical models

The multiphase momentum and energy exchange models used by the Ares code were validated by comparing the single particle position and temperature history obtained from the Ares simulation with the analytical solution as given by Colutman⁵¹. The analytical

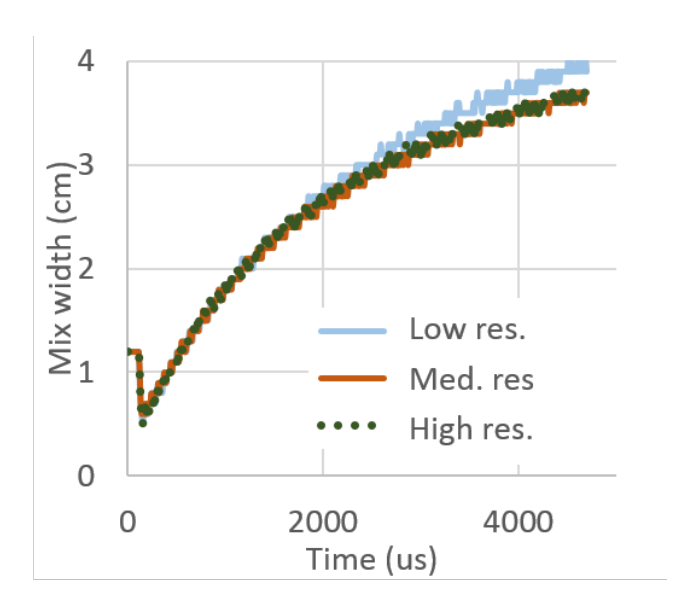


Figure 3. Mixing width over time for the three different resolution simulations.

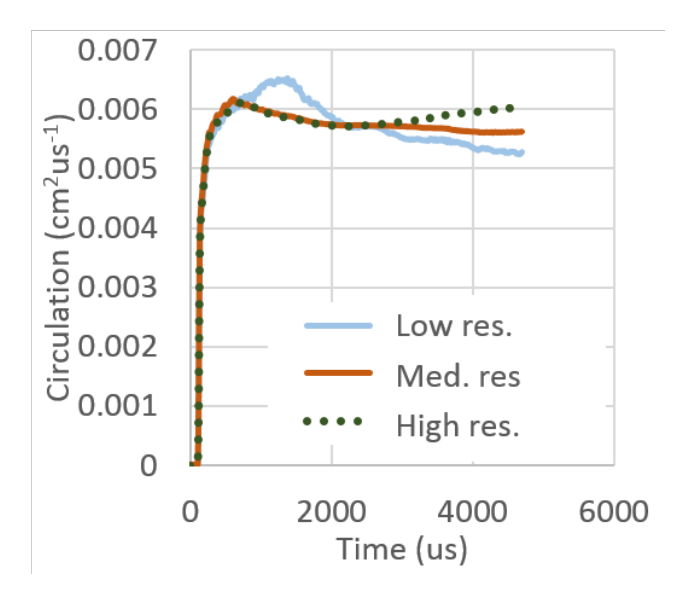


Figure 4. Positive circulation over time for the three different resolution simulations.

solution is derived considering the motion of a single particle in a fluid with the flow velocity and gas parameters like temperature, viscosity, thermal conductivity and specific heat set to be constant. A similar flow field condition was created in Ares by setting the temperature and pressure of the gas field to be 400K and 101.3kPa, with a constant viscosity and Prandtl number of 2.2027P and 0.7, respectively. Four different particle diameters, $5\mu m$, $2\mu m$, $0.5\mu m$, and $0.25\mu m$, were selected so as to perform the comparison for four different Reynolds numbers. The particle temperature was initially set to 300K, and the particle

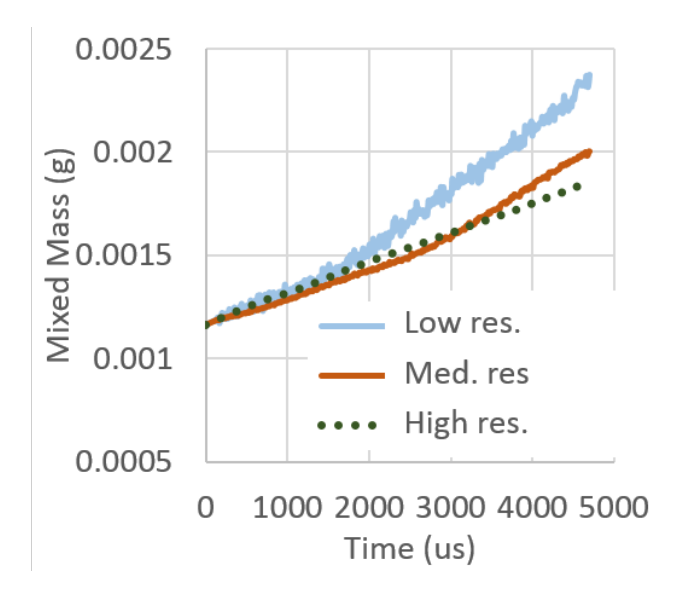


Figure 5. S2 mixed mass over time for the three different resolution simulations.

density remained constant at $1100kg/m^3$. The Reynolds number remained below 1000 at all times for each of the four cases, so only the low speed solution of the analytical equations for temperature and position history were calculated as given by equation 27 and equation 28^{51} .

$$T_p(t) - T_q = [T_p(t_1) - T_q] \exp\{-E(t - t_1) - E * F[f(v(t) - f(v_1))]\}$$
(27)

$$x(t) - x_1 = \frac{3}{B * C} \left[v_0^{\frac{1}{3}} - v(t)^{\frac{1}{3}} + C^{-\frac{1}{2}} * \tan^{-1} \left(C^{-\frac{1}{2}} * v_0^{-\frac{1}{3}} - C^{-\frac{1}{2}} * \tan^{-1} \left(C^{-\frac{1}{2}} * v(t)^{-\frac{1}{3}} \right) \right]$$
(28)

Here, T_p is the temperature of the particle, T_g is the temperature of the fluid, v_0 is the particle velocity at t=0, and x is the position of the particle. The function f(v) and constants A, B, and C are calculated as given by Cloutman⁵¹. The resulting temperatures and velocities were scaled for each particle size so that the values were in the range of 0 to 1 by using equations 29 and 30. In these equations, T_s is the scaled temperature, x_s is the scaled position, and $x(t=\infty)$ is the position of the particle when it comes to complete rest.

$$T_s = \frac{T_p(t) - T_p(t=0)}{T_p(t) - T_g}$$
 (29)

$$x_s = \frac{x(t) - x(t=0)}{x(t=\infty) - x(t)}$$
(30)

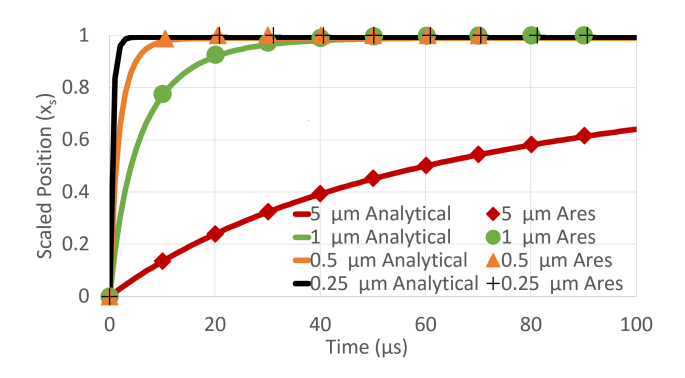


Figure 6. The scaled position history of $5\mu m$, $2\mu m$, $0.5\mu m$ and $0.25\mu m$ particles. The solid line is the analytical model and the markers represent the Ares simulation result.

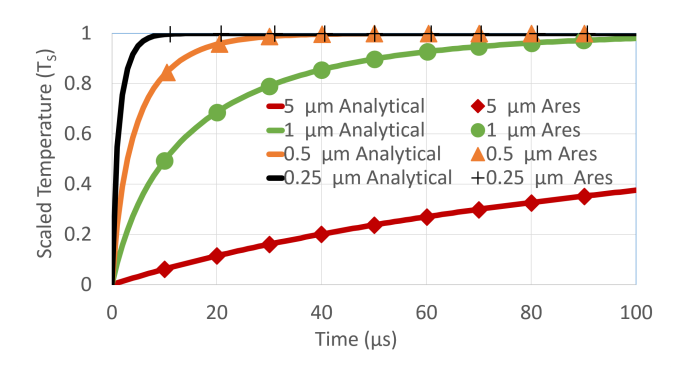


Figure 7. The scaled temperature history of $5\mu m$, $2\mu m$, $0.5\mu m$ and $0.25\mu m$ particles. The solid line is the analytical model and the markers represent the Ares simulation result.

The results obtained are summarized in figure 6 and figure 7. In the figures, the solid line represents the results of analytical solution whereas the markers represent the Ares results. It can be seen from the figure that the solid line and the markers overlap each other, which implies that there is negligible error between the position and temperature history calculated by Ares and the analytical solution. The calculated error at each of the Ares solution points is less than 0.1%. This low error is to be expected as the ares simulation is being conducted under nearly 1D conditions which closely match the case for which the analytical solution was developed.

IV. PHASE COUPLING EFFECTS

Before examining the effect of relevant parameters on the shock driven particle-gas instability, we wish to highlight the phase coupling effects which drive the multiphase instability and compare it to an equivalent classic RM instability. To do this, we will examine the development of the exemplar case with non-physical phase coupling scenarios to isolate the effects of energy and momentum coupling and compare the fully coupled simulation to a dusty gas approximation, defined in section II.

A. Energy coupling

We examine the effects of energy coupling briefly by comparing simulations with oneway, gas-to-particle, and two way energy coupling. We also examine the effect of the drag heating terms which result from changes in the particle volume fraction independent of the energy source term (eq. 17). To set the energy coupling to be one-way, we add a multiplier to the particle source term, Q_s , in equation 17 and set it to zero. One effect of this is to modify the temperature field of the gas and particles (fig. 8). The temperatures for the gas and particles are much higher in the one-way coupling simulation as the gas is unable to experience the particle cooling effects. Alternating patches of hot and cold gas are noticeable near the bubble front which are created by particle stretching. Essentially, the finite number of particles on the Lagrangian mesh are stretched in this region to a point where there are no particles in or near many zones of the gas mesh. This exaggerates the particle drag effects in regions where the particles are concentrated. We can examine the effects of particle volume by setting the gas volume fraction, ϕ_{vg} , to 1 in all equations. By removing the particle volume effects, we see that these alternating hot and cold spots and the temperature waves which exist in the spike structure are removed. This also reduces the particle and gas temperature at the interface. With particle volume effects enabled, heating of the gas can be accomplished by drag heating where part of the kinetic energy of the gas relative to the particle is converted into thermal energy as it stagnates at the particle. The drag heating effects are important, and so to retain them and eliminate the alternating hot and cold spots, we would need to split the Lagrangian particle mesh in an adaptive manner similar to the AMR employed on Eulerian gas mesh. This ability is under development

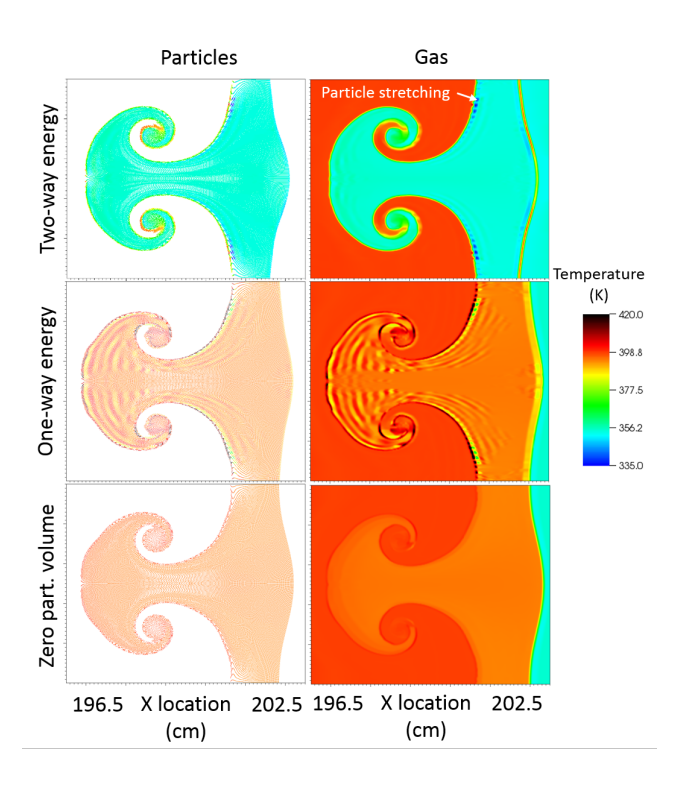


Figure 8. Comparison of simulations with two-way and one-way energy coupling and with and without particle volume effects at $\tau=200$. Left: Particle temperatures. Right: Gas temperature. Top: Simulation with two-way energy coupling. Middle: Simulation with one-way, gas-to-particle, coupling. Bottom: Simulation with one-way, gas-to-particle, coupling, and no particle volume effects, drag heating.

and will be employed in future work. For now, we note that this nonphysical temperature distribution exists only in a localized region, which does not effect the hydrodynamics, and that the physical temperature can be viewed as the average of the alternating hot and cold spots.

The two-way energy coupling also acts to increase the density of the carrier gas through particle cooling effects which results in an increase in circulation as seen in figure 9. The circulation increases sharply during passage of the shock through the interface ($t \approx 140ms$) then continues to increase at a lower rate from particle momentum deposition during momentum equilibriation (up to $t \approx 240ms$). This circulation then diffuses and spreads out for some time before beginning to dissipate (at $t \approx 600ms$). As the particles equilibriate with the gas flow, they create an effective density difference which drives additional baroclinic-like vorticity deposition. This density difference is enhanced by the particle cooling effects, which

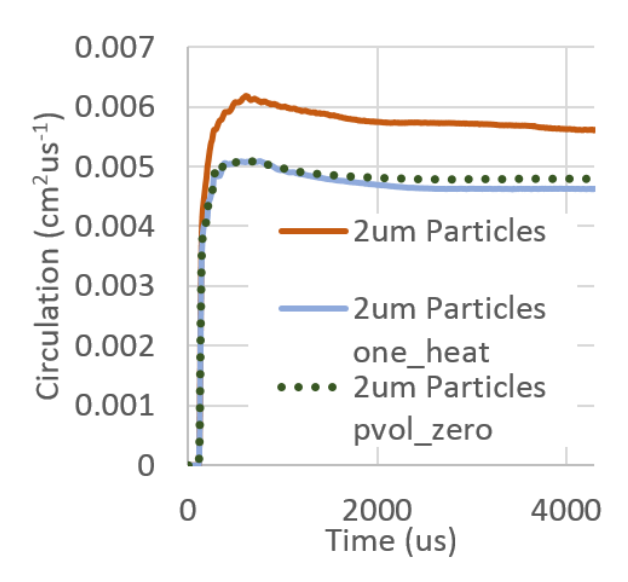


Figure 9. Comparison of circulation over time for simulations with two-way and one-way energy coupling and with and without particle volume effects.

increase the gas density, and lead to greater vorticity deposition through the baroclinic and particle vorticity source term (discussed in sect. IVB). At late times, the higher density difference created by two-way energy coupling could result in secondary vorticity deposition in the vortex cores as a result of Rayleigh-Taylor like secondary instabilities^{45,50}. Particle volume effects results in a lower circulation at late times as the drag heating converts part of the particle kinetic energy into heat. Through this method, even small particles can create additional circulation dissipation at late times.

B. Momentum coupling

To examine the effect of momentum coupling on the instability, we compare the exemplar case to a one-way, gas-to-particle, momentum coupled simulation. Figure 10 shows a clear difference between the two cases that, without two-way momentum coupling, the instability is unable to develop. This should not be a surprise, as the gas interface alone has no density difference to drive a RM instability. The effect of momentum coupling from the particles to the gas is to allow the particles, which respond at different times and have a finite relaxation time, to create a velocity difference in the gas. This velocity difference drives the interface to stretch and creates a shear that drives strong vortex development. This vorticity source can be derived by taking the curl of eqn. 16. This add a particle vorticity source term to

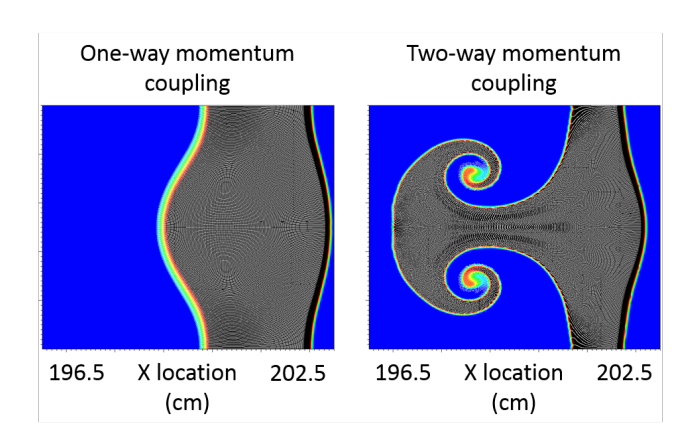


Figure 10. S2 mass fraction field and particle locations for simulations with one-way (left) and two-way (right) momentum coupling at $\tau = 200$.

Table II. Ideal gas parameters for particle and dusty gas simulations

| case | R (kJ/kg - K) | γ |
|----------------------|---------------|----------|
| particle (in N_2) | 0.297 | 1.400 |
| dusty gas | 0.237 | 1.204 |

eqn. 1, which is given by $\overrightarrow{\bigtriangledown} \times \overrightarrow{f}$.

C. Comparison to the classical RM instability

To examine the difference between the multiphase instability and Richtmyer-Meshkov instability, we will compare the exemplar case to the dusty gas approximation, the classical RM equivalent. In the limit of very small particles, the characteristic relaxation times will become negligible, and the multiphase instability will approach the dusty gas approximation as seen in section VI. For the particle-gas system, we use the exemplar case, particle diameter $2.0\mu m$ and $St \approx 0.023$, while the dusty gas is modeled with the equivalent preshock gas constant (eq. 13) and preshock ratio of specific heats (eq. 14). A summary of the gas properties for each case is shown in table II.

Figure 11 shows the evolution of the particle and dusty gas cases. The time is non-dimensionalized as described in section III C and shown in equation 23. The dusty gas approximation shows an interface that evolves as a classical RM instability with strong

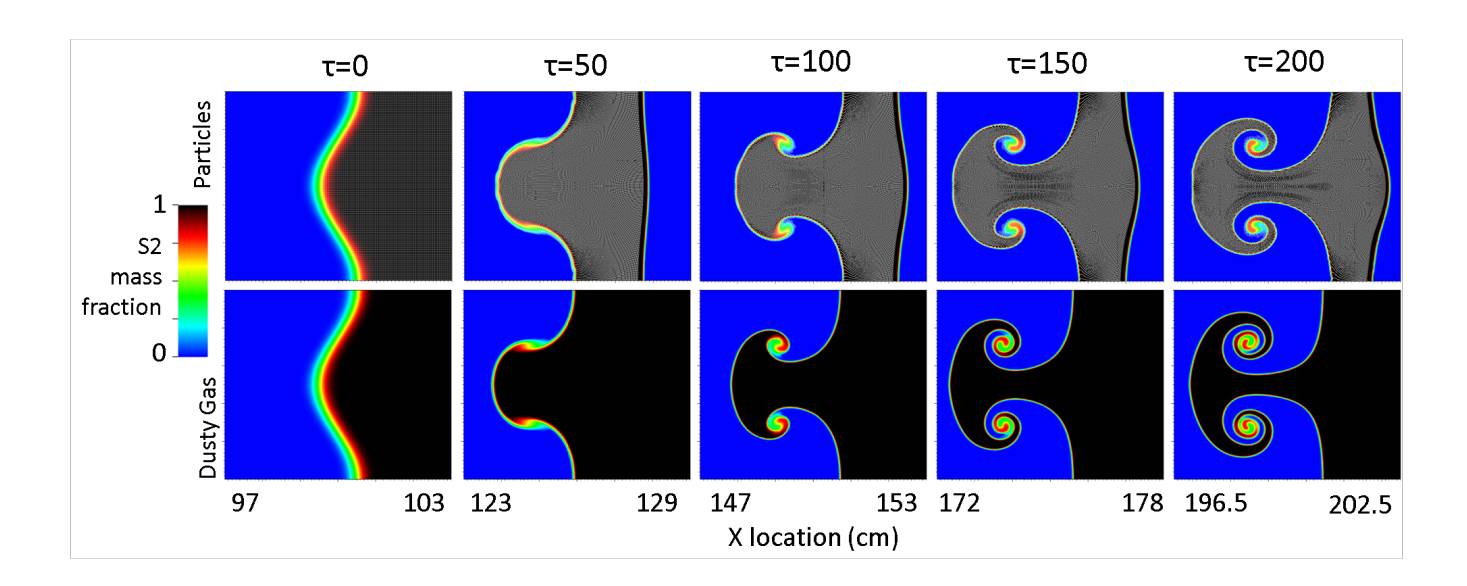


Figure 11. S2 mass fraction and particle locations for simulations at five different non-dimensional times. Top: Simulation with particles. Bottom: Simulation using the dusty gas approximation.

counter rotating vortices, while the case with particles shows weaker vortices with a thicker stem and flatter front to the spike structure and a more inclined, pointed, bubble front. The relaxation distance is visible after $\tau = 50$ at the right edge of S2 region. Particle lag is also visible in the vortices where the particles are expelled from the vortex cores by the centripetal acceleration. Overall, though, the particles seem to track the gas that they were initialized in well.

In figure 12, it can be seen that the vorticity field is disturbed by the presence of particles and that the vortex cores are weaker and more diffuse in the particle case. The temperature field shows a relatively similar development except in the particle case where the vortex core shows little thermal diffusion. The particle case also exhibits alternating cold and hot regions in S2 at the bubble front due to the particle stretching discusses in section IV A. A hot layer of gas in S2 near its interface with S3 is also visible. This area is the result of the particle relaxation distance which left an area of S2 without the cooling effect of the particles. This region does not have an opportunity to interact with the hydrodynamic interface.

The mixing width of the perturbation, as seen in figure 11, appears to be very similar for the two cases throughout their development while the mixing width plot shows the particle case has a slightly larger mixing width at late times (fig. 13). Figure 14 shows that the

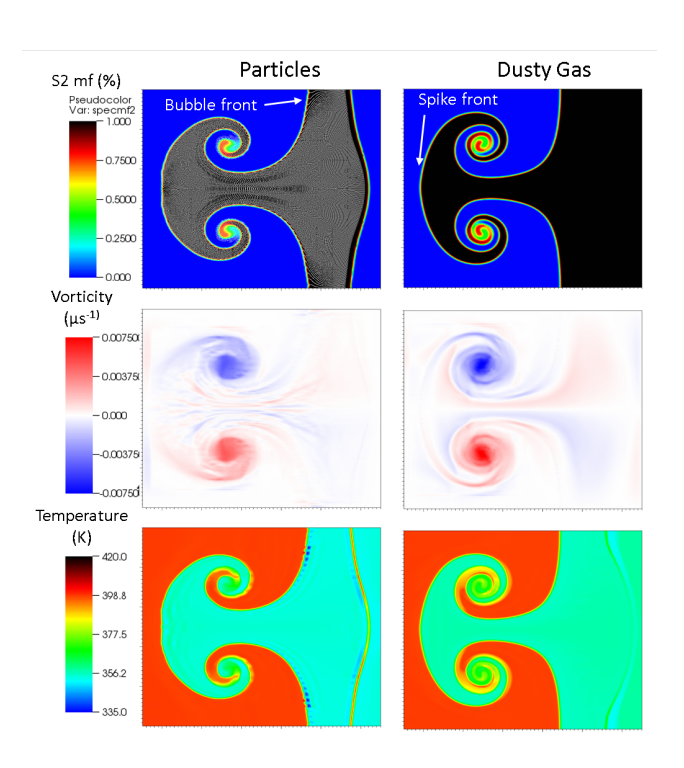


Figure 12. Comparison of the particle and dusty gas simulations at $\tau = 200$. Left: Simulation with particles. Right: Simulation using the dusty gas approximation. Top: S2 mass fraction and particle locations. Middle: Vorticity. Bottom: Gas temperature.

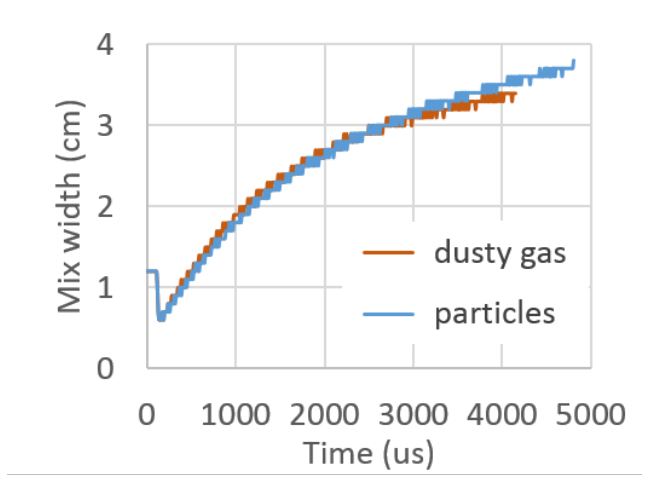


Figure 13. Mixing width over time for the particle and dusty gas cases.

circulation deposition, defined in equation 24, is diminished by approximately 25% due the particle lag effects which also reduce the amount of mixed mass (eq.25) created in the particle case by approximately 20% (fig. 15).

The particle momentum and energy coupling also have an effect on the particle tem-

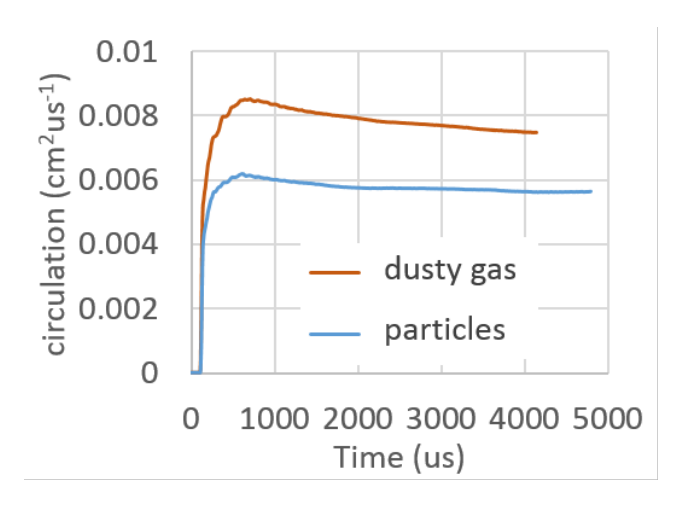


Figure 14. Circulation over time for the particle and dusty gas cases.

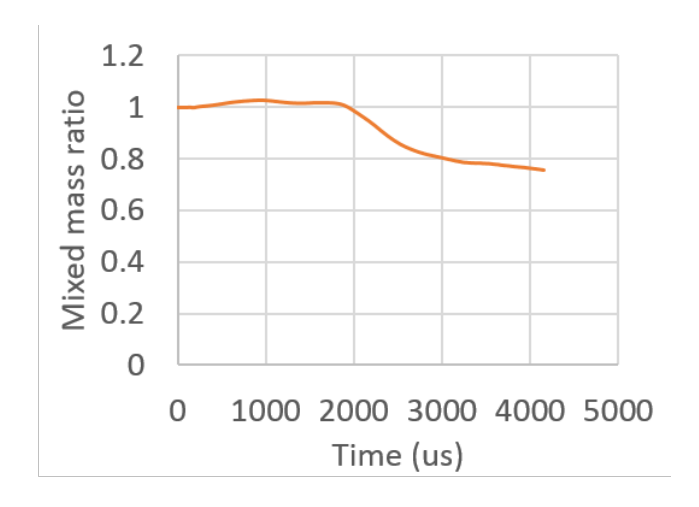


Figure 15. Ratio of the particle mixed mass to the dusty gas mixed mass over time.

peratures when compared to passive tracer particles in the dusty gas. In simulations of multi-phase astrophysics events, such as supernova dust processing, the use of passive Lagrangian particles in a dusty gas approximation of the multi-phase system⁸ is an attractive option to reduce computational times. However, particle-gas coupling can create a notice-able difference in the particle distribution and temperature history. The particle temperature distribution at late times (fig. 16) shows that a hot layer of particles develops which is entrained into the vortices. A sample of these particles (locations shown in figure 16) were traced over time to show the temperature history. The temperature history of the particles (fig. 17) shows that particles located at the hydrodynamic interface are heated to higher temperatures, as they have the fewest adjacent particles to aid in cooling the gas phase,

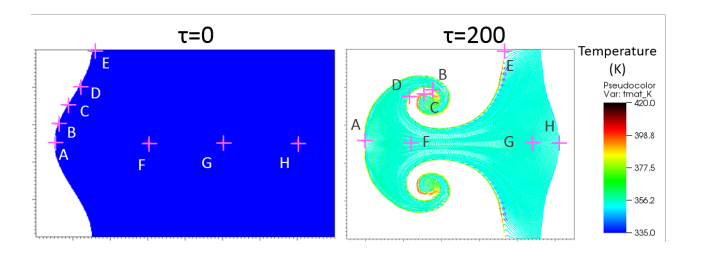


Figure 16. Sample tracer particle locations and temperatures at $\tau = 0$ and $\tau = 200$.

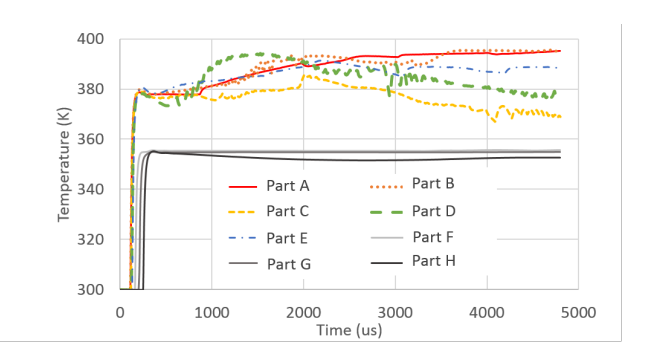


Figure 17. Sample particle temperatures over time for the particle-gas coupled simulation.

and they are able to lag behind S2 and enter S1. Passive Lagrangian tracer particles were used in the dusty gas simulation to find the equivalent particle histories. The ratio of the particle temperatures for the particle-gas coupling and dusty gas cases is shown in figure 18 for particles initialized on the hydrodynamic interface. This figure shows that the particle temperatures stay within 10% of the dusty gas approximation and that the particle temperatures are mostly higher when momentum and energy coupling are considered. Particles that were not initialized on the hydrodynamic interface showed less than a 1% deviation between the two cases.

V. SHOCK STRENGTH EFFECTS

The effects of shock strength on the particle driven instability is examined briefly in this section by comparing the Mach 1.5 exemplar case to a Mach 3.0 simulation with all other initial conditions being the same. Due to the stronger compression effects of the high Mach number shock wave, the initial particle field is extended for the Mach 3.0 case to ensure no interaction of the hydrodynamic interface with the downstream S2-S3 interface. The Atwood numbers remain the same, but the stronger shock strength increases the particle

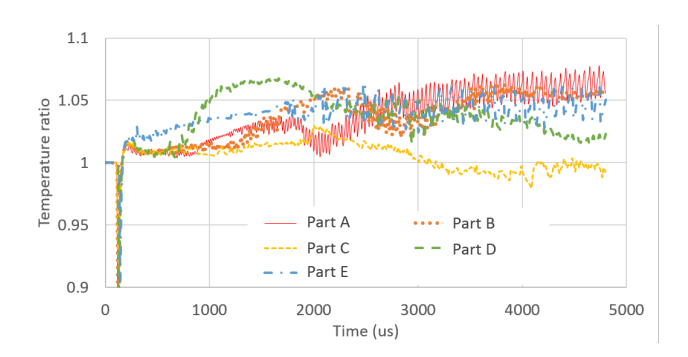


Figure 18. Ratio of the sample particle temperatures over time for the particle-gas coupled and dusty gas simulations. A ratio over one indicates higher temperatures for the particle-gas coupled simulation.

Stokes number and characteristic time ratios slightly ($St \approx 0.08$, $\tau_V \approx \tau_T \approx 0.14$). Figure 19 shows the Mach 3.0 simulation species and vorticity fields at a non-dimensional time of 200 (compare to Mach 1.5 case in figure 12) for both the particle and dusty gas cases. From the species field, it can be seen that for a Mach 3.0 incident shock strength, the particle coupling effects have a diminished effect. The particle case shows a thicker spike stem and a more pointed bubble front as before. The votricity plots show that the distribution in vorticity and strength is more similar in the Mach 3.0 cases. The dusty gas case shows slightly stronger vortex cores, but the strength within the pike structure is much more similar than in the Mach 1.5 cases. Figure 20 shows positive circulation over time for the four cases. At late times, the Mach 3.0 dusty gas case shows an approximately 20% increase over the particle case, while for the Mach 1.5 cases there is an approximately 33% increase at late times.

Additional features are made visible by plotting the particles by their original X locations as seen in figure 21. In this figure, a reverse jet can be seen which pulls particles towards the downstream edge of the interface. This feature is also found in RM instabilities^{52,53}. The particles that start near the hydrodynamic interface are largely drawn into the vortices. In the Mach 3.0 case, the reverse jet has sufficient strength to fully invert the X positions of particles near the center of the spike.

As the incident Mach number is increased, the temperature distribution of the particles widens. Particle temperatures were traced over time as described in section IV C, and particles with the same initial location as shown in figure 16 were used. The late time positions of these sample particles are shown in figure 22. Surface particles reach temperatures up

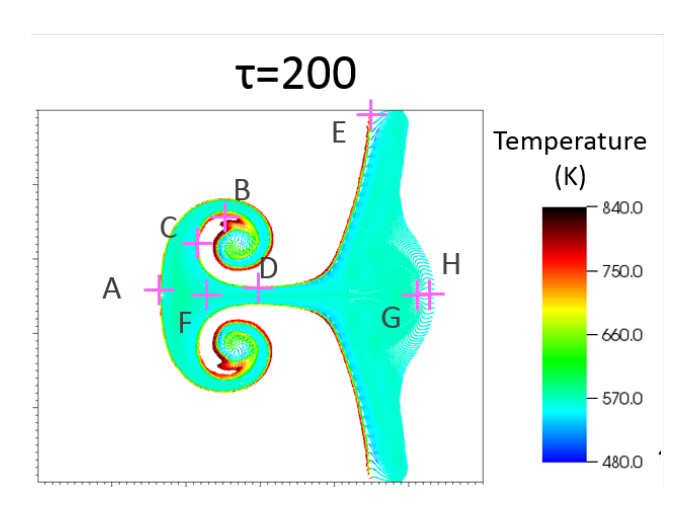


Figure 19. Comparison of the particle and dusty gas cases for an incident shock strength of 3.0. Top: species and particle positions. Bottom: vorticity fields. Left: Particle simulation. Right: dusty gas simulation.

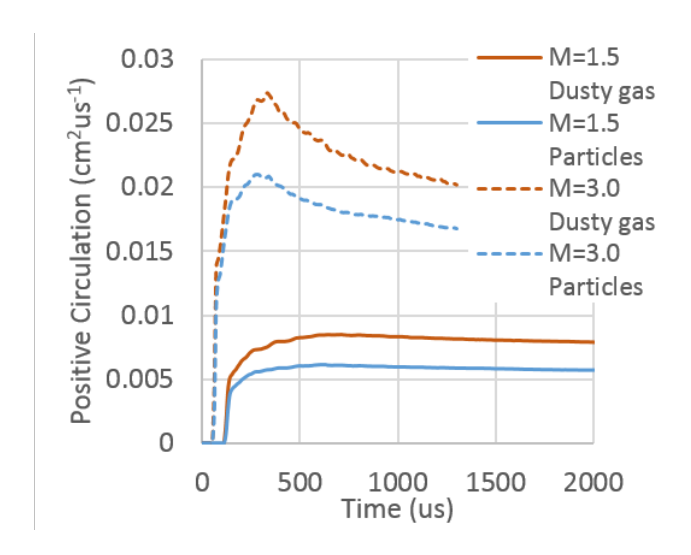


Figure 20. Circulation over time for the Mach 1.5 and Mach 3.0 particle and dusty gas cases.

to 840 K while interior particles remain near 560 K (fig. 23). As before, Lagrangian tracer particles were used in the dusty gas simulations to highlight the differences in particle temperatures due to particle-gas coupling effects. The ratio of the particle temperatures in the two simulations shows that as Mach number increases, the effects of phase coupling create a larger error in temperature, up to 21%, due to the use of the dusty gas approximation (fig. 24). While the particle characteristic thermal time ratio increased slightly for the Mach 3.0 case, approximately 13%, we do not believe this is enough to explain the increase in particle

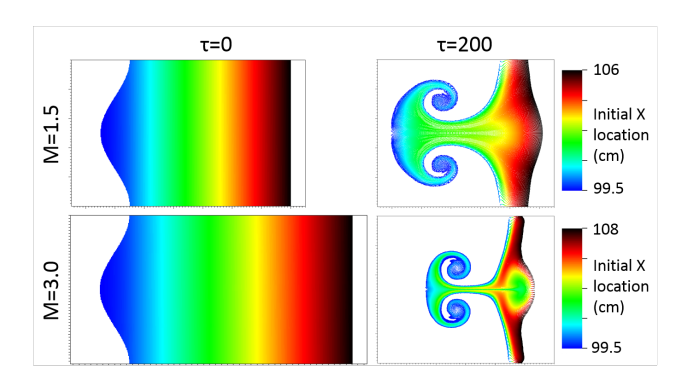


Figure 21. Comparison of the particle initial X positions at $\tau = 0$ and $\tau = 200$. Top: Mach 1.5 simulations. Bottom: Mach 3.0 simulations. Left: $\tau = 0$. Right: $\tau = 200$.

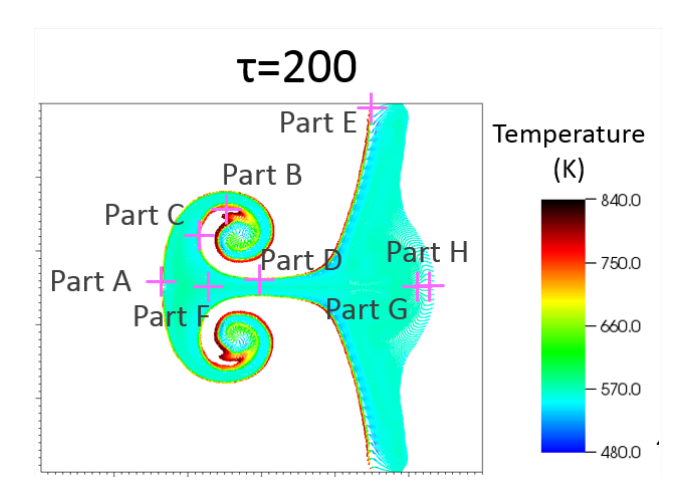


Figure 22. Sample tracer particle locations and temperatures at $\tau = 0$ and $\tau = 200$ for the Mach 3.0 shock wave simulation.

temperature ratios. We can see from the data in this section that for stronger accelerations the circulation is less affected while the particle temperatures are more affected by the particle-gas coupling.

VI. PARTICLE SIZE EFFECTS

Having briefly considered the effect of incident shock strength on the particle-gas hydrodynamic instability, we now examine the effect of particle size on the exemplar case ($A_g = 0$, $A_{pg} = 0.11$, Mach 1.5). We add to the previous simulations two more cases with increasing particle sizes and one case with a smaller particle size while maintaining the same Atwood numbers. We will refer to these cases by the particle diameters using the descriptors in table

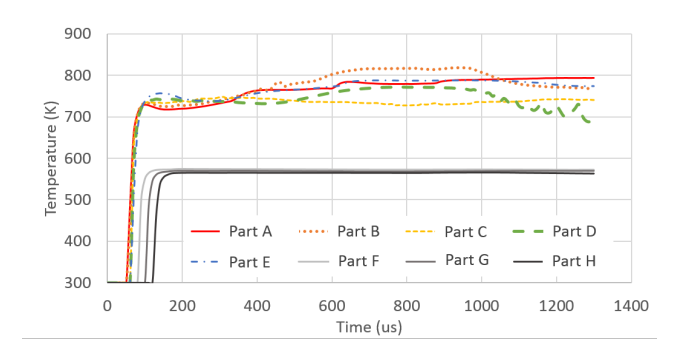


Figure 23. Sample particle temperatures over time for the particle-gas coupled simulation with a Mach 3.0 shock wave.

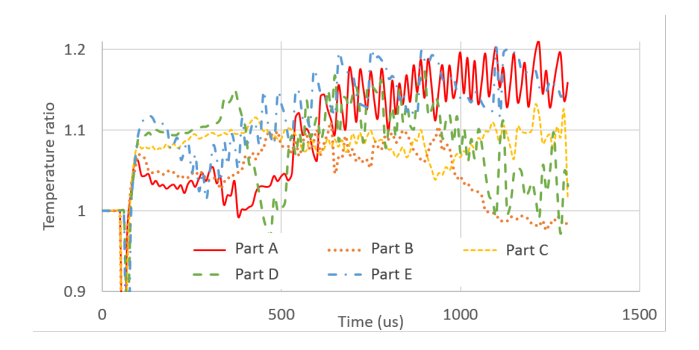


Figure 24. Ratio of the sample particle temperatures over time for the particle-gas coupled and dusty gas simulations with a Mach 3.0 shock wave. A ratio over one indicates higher temperatures for the particle-gas coupled simulation.

III, which summarizes the simulation variables. The particles sizes span from very small characteristic time ratios ($\tau_{V/T} \approx 0.01$) to larger values ($\tau_{V/T} \approx 3.0$).

For the large particle simulations, it was necessary to extend the S2 region, which con-

Table III. Particle size study case descriptions.

| case name | $d (\mu m)$ | St | $	au_V$ | $	au_T$ |
|------------------|-------------|--------|---------|---------|
| dusty gas | na | 0 | 0 | 0 |
| exemplar case | 2 | 0.023 | 0.119 | 0.121 |
| small particles | 0.5 | 0.0014 | 0.00747 | 0.00755 |
| medium particles | 4.5 | 0.121 | 0.605 | 0.611 |
| large particles | 10 | 0.597 | 2.986 | 3.020 |

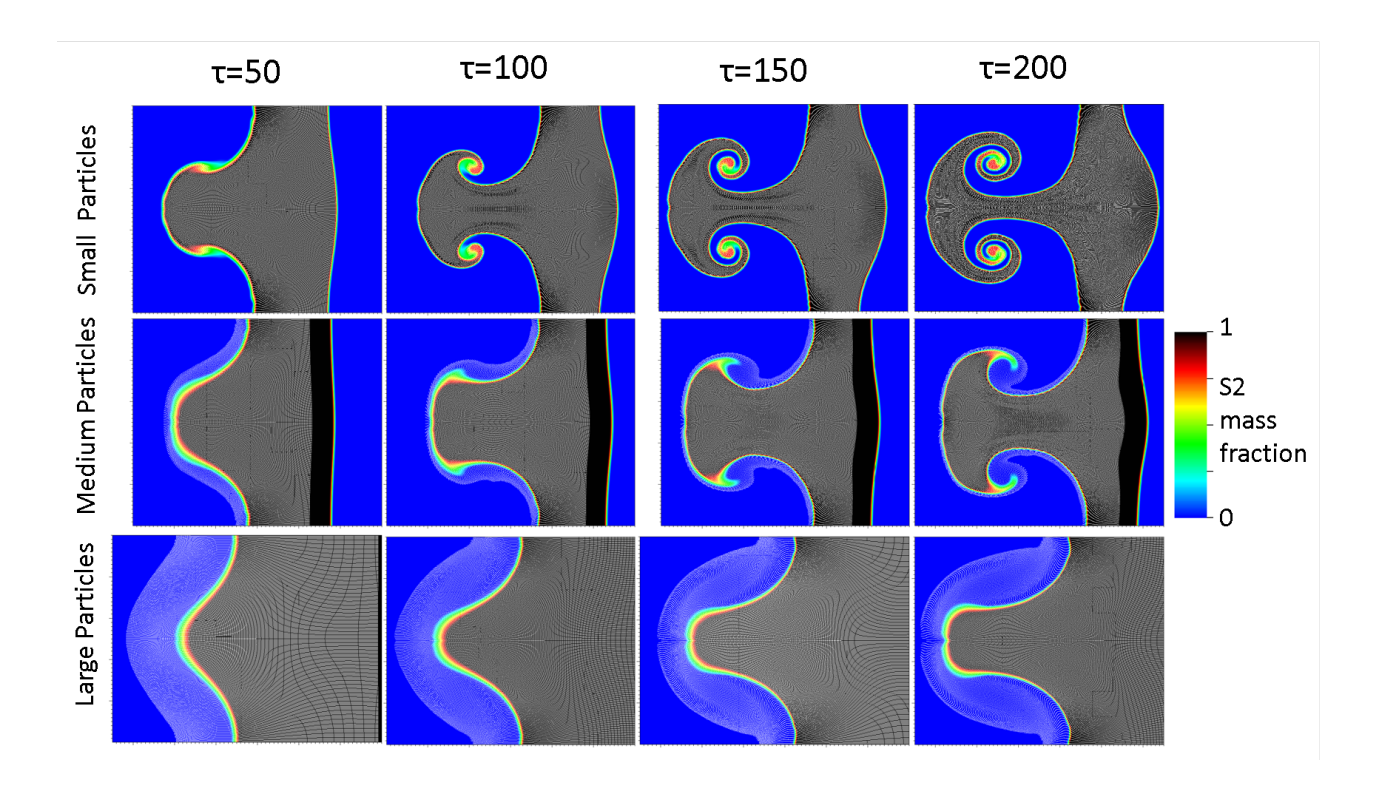


Figure 25. S2 mass fraction and particle locations for the particle size simulations at four different non-dimensional times.

tained the particles, due to the larger particle lag distance. Figure 25 shows the development of the interface with the three different particle sizes. This figure shows that a significant particle lag is created for the large particles, with the particle cloud extending well into S1. The larger particles also slow the entire interface down by a small amount as it travels downstream, which can be seen in the fact that at late times the large particle interface is centered slightly to the left of the other interfaces (all images have the same X coordinate at the left edge). The most noticeable effect is clearly the lack of vortex development as the particle size is increased. The overall height of the interface is similar in all cases, but the stretching of the interface, and therefore the molecular diffusion potential, is reduced considerably due to the lower vorticity in the larger particle cases. The small particle case shows a development which is more similar to the dusty gas case than the exemplar case.

Figure 26 shows several variable fields at $\tau = 200$. The vorticity fields show that the vortex strength is greatly diminished for the large particle case and that the vortex cores are unable to develop. The gas temperature fields show that the large particles extend their cooling effect into the S1 region. As before (sect. IV A), there are some cold regions of

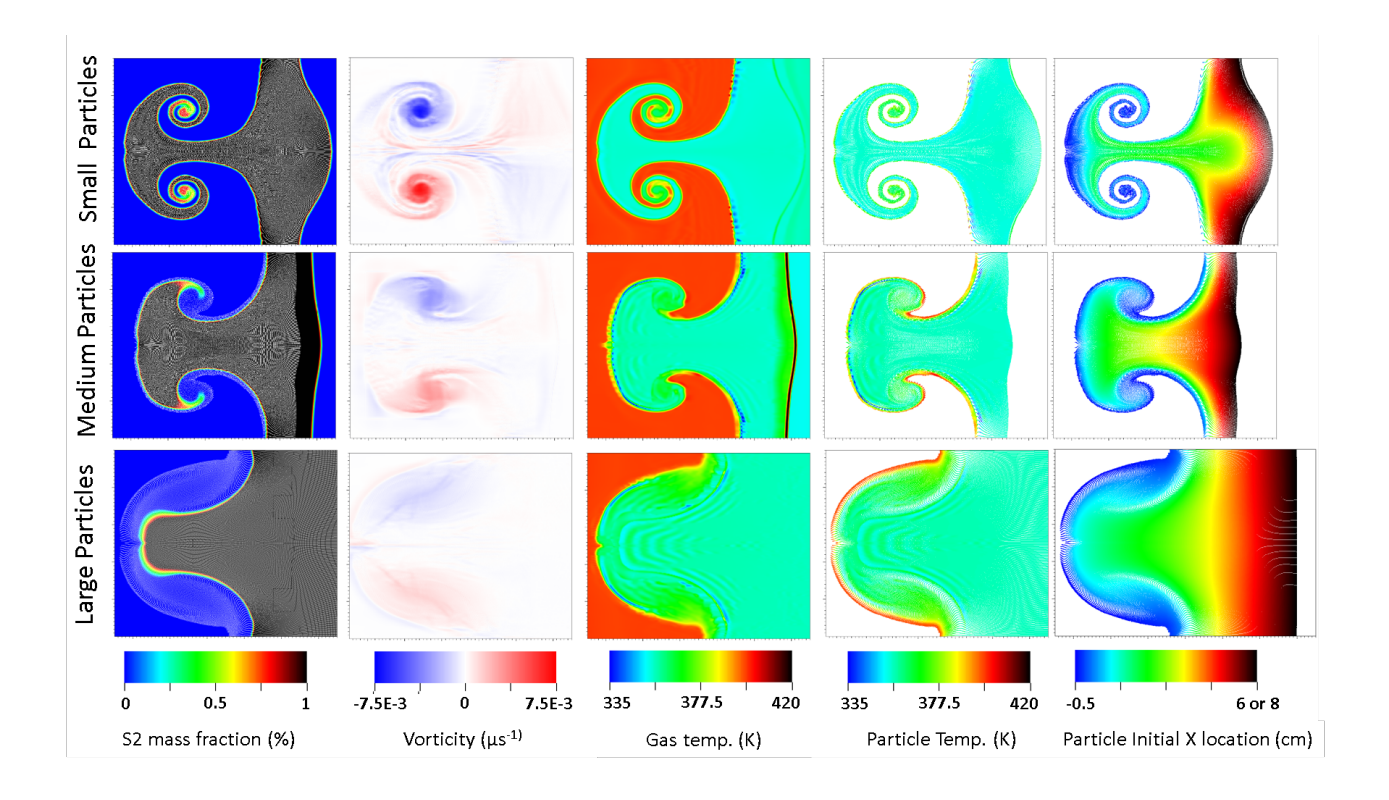


Figure 26. Pseudocolor plots of variable fields at $\tau=200$ for the three different particle size cases. Top: Small particles. Middle: Medium particles. Bottom: Large particles. Left: S2 mass fraction and particle locations. Left Center: Vorticity field. Center: Gas temperature field. Right Center: Particle temperatures. Right: Particle initial X locations (note the X location color bar extends to 6 cm for the medium and small particles and to 8 cm for the large particles).

gas created by numerical effects due to stretching of the Lagrangian particle field and the particle volume effects. The particle temperature fields show that there are a greater number of hot particles which are arranged in a thicker sheet and not entrained into the vortices as in the small particle case. This indicates that, for larger particle relaxation times, a larger number of particles may have temperatures which deviate significantly from the dusty gas approximation but that their distribution may be more uniform. The plots of particle initial X location show that the weak reverse jet seen in the small particle and exemplar cases is completely damped for the medium and large particle cases.

The upstream most (lowest X distance) particle location and S2 location vary significantly in the large particle case. For this reason, we now define a particle mixing width as the distance from the upstream most particle to the 95% contour of S2 at the spike tip. This amounts to the distance which the particles have penetrated into S1 at the spike tip created

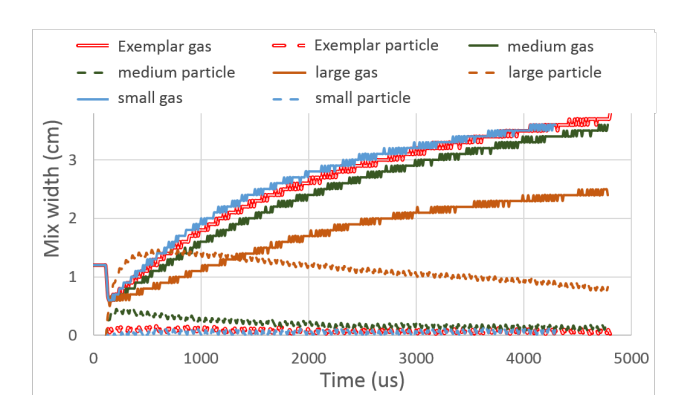


Figure 27. gas and particle mixing width over time for the different particle size and the dusty cases.

by S2. Figure 27 shows both the gas and particle mixing widths over time for the four cases. This figure shows that the particle mixing width peaks at early times and then declines in time as the gas hydrodynamics cause the gas interface to grow and recover some of the initial particle lag distance. All but the large particle case have negligible (< 0.1 cm) particle mixing widths at late times. The gas mixing widths for the small and medium particle cases are very similar to the exemplar case and the dusty gas case seen in section IV C. The large particle case, however, shows a significantly damped gas mixing width ($\approx 1 \text{ cm}$ less), but if the particle mixing width at the spike tip is included, this combined mixing width would be similar to the dusty gas case.

Figure 28 shows that the circulation decreases steadily with increasing particle size. All cases except the small particle case show a significantly lower circulation than the dusty gas case. For the small particle case, the initial circulation deposition is equal to that of the dusty gas case. However, it decays faster at late times due to the particle drag effects discussed in section IV A. This highlights the effect of particle drag and shows that the initial circulation deposition converges to that of the dusty gas case for particles with short relaxation times, as expected. The reason for the reduction in circulation can be attributed to the advection of the particle vorticity source term. This source term can be derived as the curl of the momentum source term $\varepsilon_{ijk}\partial_j f_k$, where ε_{ijk} is the alternating unit tensor. The advection of the vorticity source term leads to a competition between the upstream vorticity, created by the flow adjusting to the particle presence, and vorticity deposited at the particle. The advection of the source term also spreads the vorticity over a larger area, aiding in its diffusion. In the limit of very small particles, there is no advection of

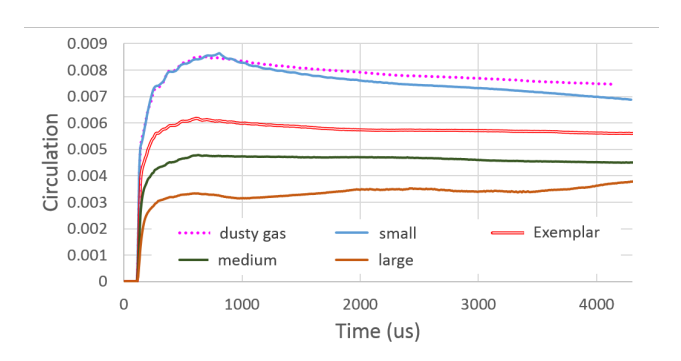


Figure 28. Circulation over time for the different particle size and the dusty cases.

the particle vorticity source term and the source term remains aligned with the vorticity deposited on the flow. An additional discussion of vorticity production and competition for 3D multiphase turbulent flows is given by Ahmed and Elghobashi⁵⁴.

The total amount of mixed mass is shown in figure 29 where we track the mixed mass of gas, defined as the mass of S2 that is in zones where the S1 mass fraction is greater than 50%, and the particle mixed mass, defined as the mass of particles where the S1 mass fraction is greater than 50%. From this figure, we can see that the gas mixed mass is similar for all particle cases. We can see that the particle size does not significantly alter the gas mixed mass from the dusty gas approximation. The particle mixed mass increases with particle size, and while the small, medium, and exemplar particle mixed mass are lower than the gas mass, the large particle mixed mass is much larger than the gas mixed mass. It is important to consider the particle mixed mass if mixing is of interest and the particle relaxation time ratios are large. We would note, however, that this effect will reverse if the interface is accelerated again in the opposite direction by a reshock. In this case, the particles can be redistributed back into S2, but we leave a detailed discussion of this for future work.

VII. ATWOOD NUMBER EFFECTS

So far the work presented has focused on hydrodynamic instabilities driven by the addition of particles in one region of a uniform gas. This results in a gas Atwood number of 0 for the interface. In this section, we will explore the combined effects of gas and particle-gas Atwood numbers. For now, we continue to limit ourselves to having particles only in the downstream species which limits us to particle-gas Atwood numbers that are greater than the gas Atwood number. We hold the particle-gas Atwood number constant at the previous

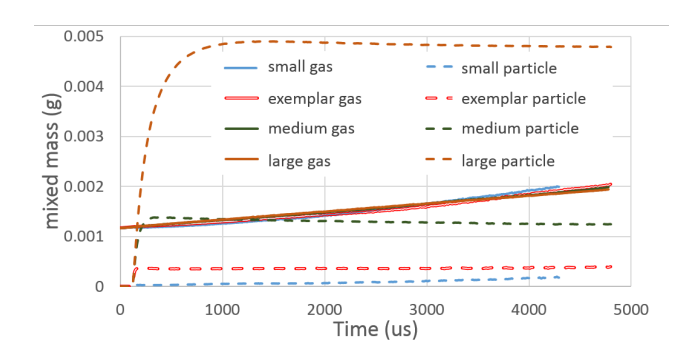


Figure 29. Gas and particle mixed mass over time for the different particle size and the dusty cases.

Table IV. Atwood number study case descriptions.

| case name | A_g | $	au_V$ | $	au_T$ | N_2 (% volume) | CO_2 (% volume) | He (% volume) |
|-------------------------|--------|---------|---------|------------------|-------------------|---------------|
| $A_g 0.055 \tau 0.1$ | 0.054 | 0.123 | 0.127 | 0.80 | 0.20 | 0.00 |
| $A_g 0.055 \tau 3.0$ | 0.054 | 3.074 | 3.171 | 0.80 | 0.20 | 0.00 |
| A_g -0.055 τ 0.1 | -0.054 | 0.118 | 0.076 | 0.88 | 0.00 | 0.12 |
| A_g -0.055 τ 3.0 | -0.054 | 2.938 | 1.908 | 0.88 | 0.00 | 0.12 |

value of 0.11 by adjusting the particle mass loading and study two gas Atwood numbers of 0.055 and -0.055, where a negative A_g signifies that the density of S1 is greater than that of S2 (eq. 2). We vary the preshock gas Atwood number by varying the gas composition and limit ourselves to compositions of N_2 , CO_2 , and He that could be achieved in experimental work. We will also consider the effects of particle size in combination with Atwood number effects by exploring two relaxation time ratios, 0.1 and 3.0. The properties of the four cases explored in this section are summarized in table IV. It should be noted that the addition of helium to the negative A_g cases causes the larger difference in velocity and thermal relaxation time ratios.

Figure 30 shows the evolution of the four different gas Atwood number cases. At small relaxation time ratios, the particle-gas Atwood number dominates the hydrodynamics. The negative A_g case at small $\tau_{V/T}$ shows slightly less developed vortices at late time and a slightly higher interface jump velocity compared to the positive A_g case. At large $\tau_{V/T}$, the gas Atwood number has a significant effect. The negative A_g case shows a much lower vortex development and a small spike structure with a similarly sized particle cloud in S1

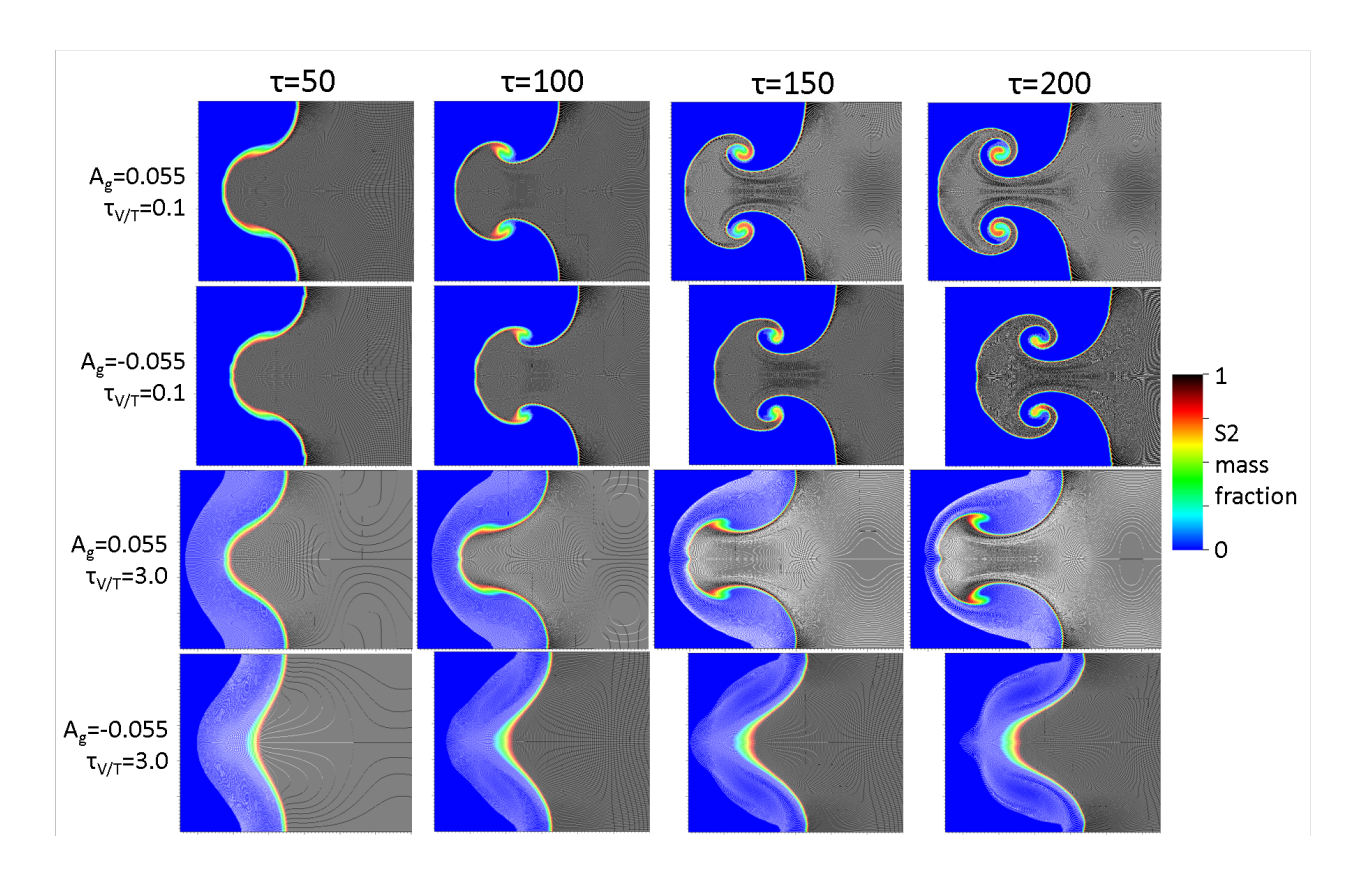


Figure 30. S2 mass fraction and particle locations for the four different A_g and $\tau_{V/T}$ cases at four different non-dimensional times. Top: $A_g 0.055\tau 0.1$. Top center: $A_g 0.055\tau 3.0$. Bottom center: $A_g - 0.055\tau 0.1$. Bottom: $A_g - 0.055\tau 3.0$

compared to the positive A_g case.

Figure 31 shows some flow field variables at $\tau=200$ for the four cases. The density and temperature fields both show the distinctive difference between a negative and positive A_g gas. The low $\tau_{V/T}$ cases show similar developments as before with nearly identical vorticity fields. Both these cases show some development of a reverse spike in the particle initial X position plots. The primary difference in these cases is the lower temperature and density for the negative A_g case. For the high $\tau_{V/T}$ cases, we see that the positive A_g case particle fields develop similarly to the large particle case in section VI which had $A_g=0$, but that the positive A_g allows for greater development of the vortices despite the particle lag distances. Both cases show no development of a reverse spike. The artificial temperature fluctuations resulting from particle stretching (sect. IV A) are magnified in the negative A_g , high $\tau_{V/T}$ case by the presence of helium in the carrier gas.

The reason for the lack of vortex development in the negative A_g case is evident in

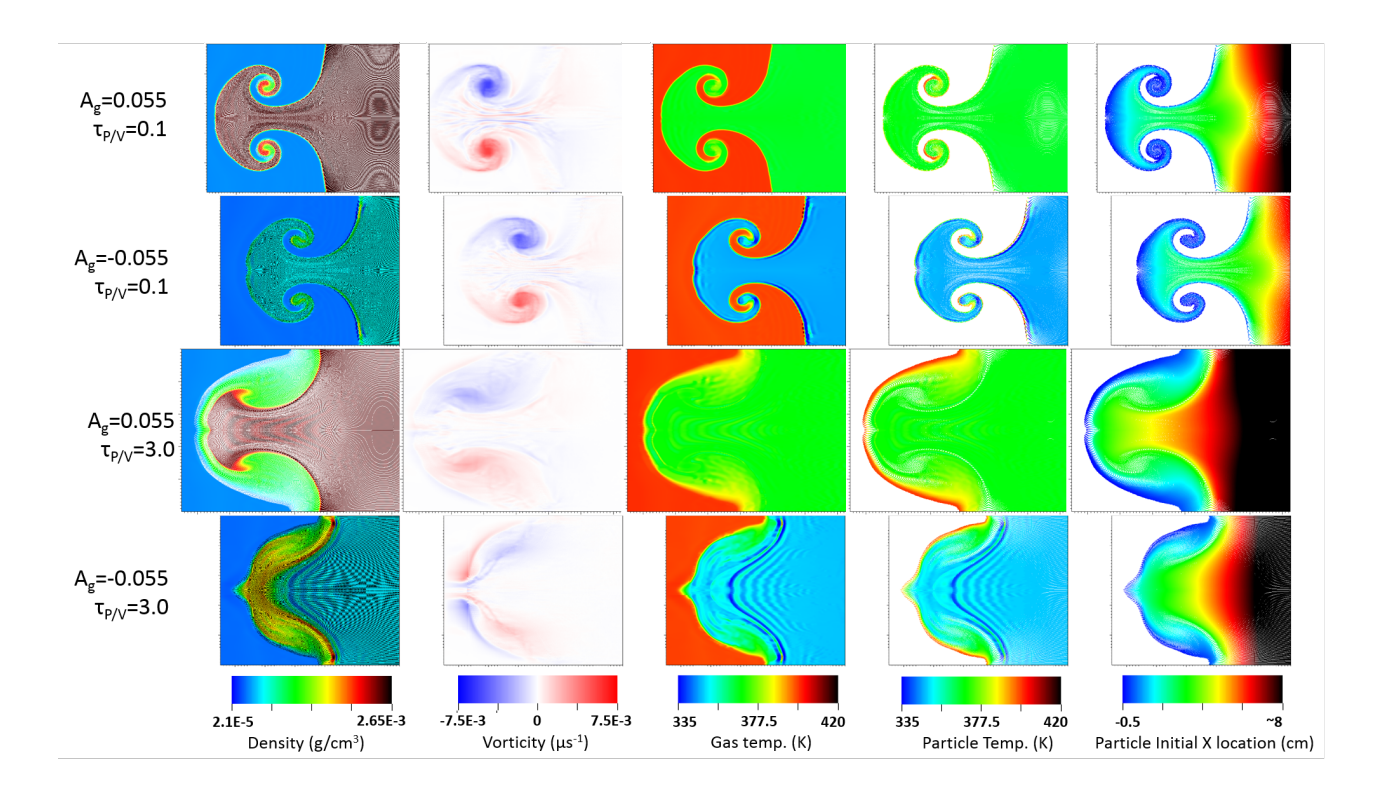


Figure 31. Pseudocolor plots of variable fields at $\tau = 200$ for the four different A_g and $\tau_{V/T}$ cases. Top: $A_g 0.055\tau 0.1$. Top center: $A_g 0.055\tau 3.0$. Bottom center: $A_g - 0.055\tau 0.1$. Bottom: $A_g - 0.055\tau 3.0$. Left: density and particle locations. Left Center: Vorticity field. Center: Gas temperature field. Right Center: Particle temperatures. Right: Particle initial X locations (note the X location color bars were scaled so that they extend to ≈ 8 cm.

the vorticity field where two vortex sheets, which are opposite in sign, can be seen at the interface. Figure 32 shows the vorticity field initially deposited on the interface for the two negative A_g cases to highlight the effect of particle relaxation times. These vorticity fields show that the negative A_g is able to create a positive (negative) vorticity layer at the top (bottom) of the interface while the particles lag behind and deposit a negative (positive) layer. These vortex sheets compete over time and eventually invert their positions as particles push out of S2 and into S1. This suggest a possible method for damping the RM instability using particle relaxation effects.

Figure 33 shows the gas and particle mixing widths as defined in section VI. This plot shows that the negative A_g case with high $\tau_{V/T}$ has a much lower mixing width than the other cases and is the only case with a gas mixing width which departs substantially from the dusty gas case. This case has a mixing width that is approximately 10% lower than

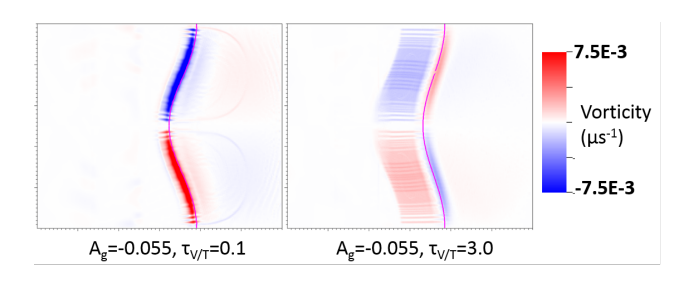


Figure 32. Vorticity deposited on the interface at $\tau \approx 5$ for the two cases with $A_g = 0.055$. The S2 50% mass fraction contour is shown as a line to highlight the interface position. Left: $\tau_{V/T} \approx 0.1$. Right: $\tau_{V/T} \approx 3.0$.

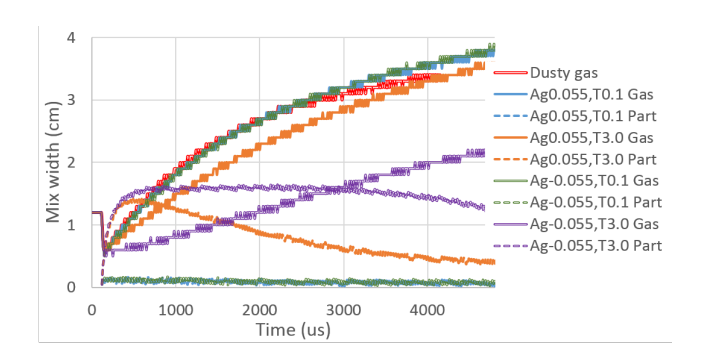


Figure 33. Gas and particle mixing width over time for the four different A_g and $\tau_{V/T}$ cases along with the dusty gas case. Note that the A_g 0.055,T0.1 and A_g -0.055,T0.1 data sets are very close and are difficult to differentiate for both the gas and particle mixing widths.

the zero A_g large particle case in section VI. The relatively small Atwood number is able to suppress some of the growth driven by the particle-gas Atwood number, and, perhaps at larger values, it may be able to suppress the instability completely. The particle mixing width is large for both high $\tau_{V/T}$ cases but quickly decays for the positive A_g case as the gas hydrodynamics draw S2 into S1 further. The positive A_g cases show some suppression of the gas hydrodynamics by the larger particles.

The circulation for the four cases is shown in figure 34 where it can be seen that all cases possess much lower positive circulation than the dusty gas case. The low $\tau_{V/T}$ cases have similar circulation despite their different A_g . The high $\tau_{V/T}$ cases show similar circulations with the negative A_g case being a bit lower at all times. This positive circulation measurement shows that, while the sum of the circulation in the flow fields is similar, the distribution has significant effects in the negative A_g case where the two vortex sheets of opposite sign

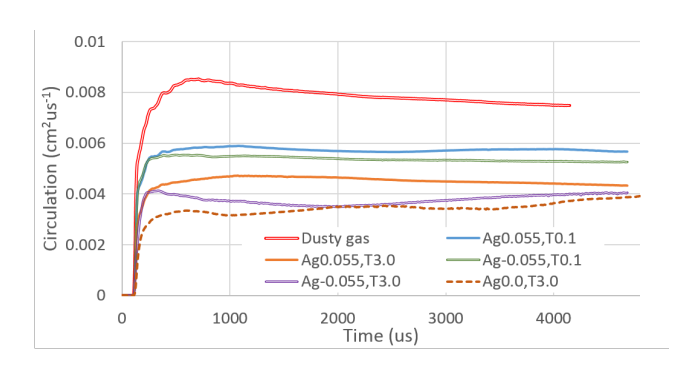


Figure 34. Circulation over time for the four different A_g and $\tau_{V/T}$ cases along with the large particle case from the previous section ($A_g = 0$, $\tau_{V/T} \approx 3.0$ and the dusty gas case.

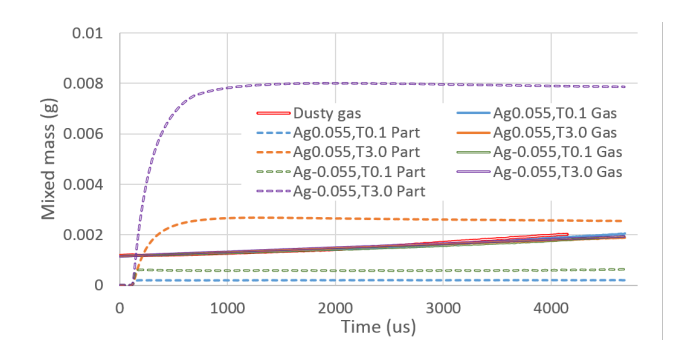


Figure 35. Gas and particle mixed mass over time for the four different A_g and $\tau_{V/T}$ cases along with the dusty gas case.

compete. The circulation for these high $\tau_{V/T}$ cases initially increases identically due to the equal and opposite A_g , but the particle effects become apparent at $\tau \approx 5$, seen in fig 34, and create a sudden small drop in circulation.

The mixed mass for the gas and particles is shown in figure 35. All cases possess a similar mixed gas mass to the dusty gas case but have different mixed particle masses. The low $\tau_{V/T}$ cases have small particle mix masses with the negative A_g case showing a slightly higher values as the gas hydrodynamics initially push S2 in the positive X direction relative to the particles. The high $\tau_{V/T}$ positive A_g case shows a lower particle mixed mass than the zero A_g large particle case from section VI due to the gas hydrodynamics which pull the gas interface in the same direction as the particles. The high $\tau_{V/T}$ negative A_g case shows the largest mixed particle mass as the particles lag significantly behind the flow and the gas hydrodynamics are damped.

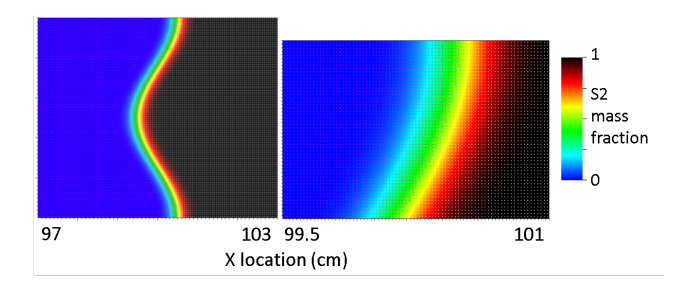


Figure 36. S2 mass fraction and particle locations for groups one (left) and two (right) at tau = 0. Left: initial interface. Right: Close up of the particle locations at the interface.

VIII. PARTICLE RELAXATION DRIVEN INSTABILITY

In this final section, we wish to briefly introduce the concept of an instability which is driven completely by variations in particle relaxation times. In the previous section, we have used a combination of A_g and A_{pg} to drive the instabilities. In this section, we will use a particle group located in S1 as well as S2. The gas Atwood number will be set to zero by using nitrogen as the carrier gas for both species. We then set two different particle sizes while holding the mass loading for each group to be 25% as in previous sections. Under these conditions, both A_g and A_{pg} will be zero by definition, though the interface will experience non-zero values temporarily due to particle lag effects, as the $\tau_{V/T}$ will be different for each particle group. In the case of S1 and S2 particle groups with slow and fast relaxation times respectively, we find that the interface will initially experience a positive A_{pg} and will evolve similarly to the previous cases. For brevity, we focus on the case of S1 and S2 particle groups with fast and slow relaxation times, respectively. This case will initially experience a temporary negative A_{pg} due to the larger particle relaxation time of the S2 particle group. The temporary A_{pg} felt by the interface due to lag effects will be limited to $\approx \pm 0.11$. At later times, as the S2 particle group equilibriates with the gas flow, the flow will respond as if it has a temporary positive A_{pg} . The initial conditions for this case are shown in figure 36.

Figure 37 shows the evolution of the particle locations and species mass fraction over time for the negative A_{pg} simulation. We see that two instabilities evolve in a way; one instability for the S2 particle group and another instability for the S1 particle-gas system. At late times, the gas interface has grown as if it had a weak negative A_g , yet the S2 particle group has grown into S1 as if it had a positive A_{pg} . This creates a large region of high

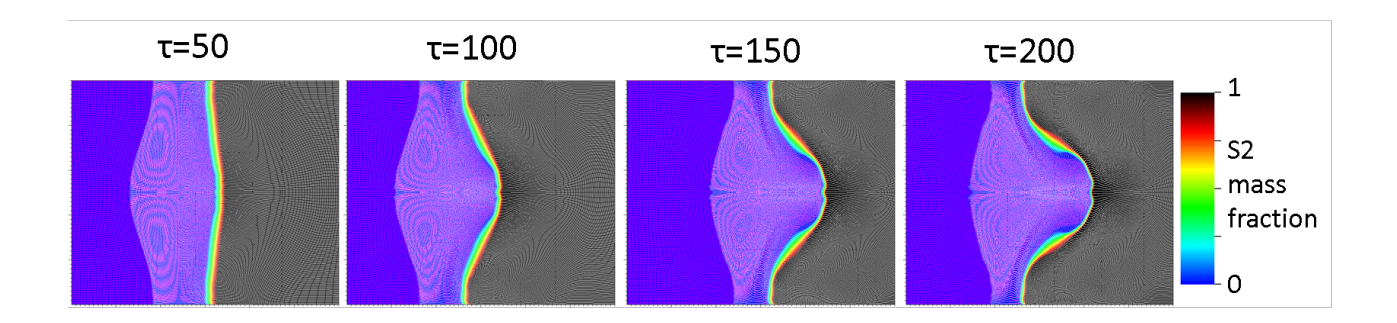


Figure 37. S2 mass fraction and particle locations for groups one (left) and two (right) at four different non-dimensional times.

particle concentration where both S1 and S2 particle groups are present.

Figure 38 shows the different variable fields for the system at $\tau = 200$. The density and temperature fields show that overlapping particle groups create a cold high density region of S1. This region could create a strong secondary instability if it were accelerated by a second shock or reshock due to its higher gas density and particle mass fraction. The particle temperature fields show that the temperature distribution is bi-modal for both particle groups, with a large group of cool particles and a group of colder particles (compared to cases in previous sections) in the overlapping region. The particle initial X locations show a RM type spike structure in the S1 particle group and a reverse spike like structure in the S2 group which is driven by particle-gas-particle coupling with the S1 group. The vorticity field shows two weak vortex sheets which are opposite in sign, as seen for the negative A_g large $\tau_{V/T}$ case in section VII. These sheets originate at early times from the initial shock interaction but possess stronger vorticity created by the initial temporary negative A_{pg} felt by the interface (fig. 39).

For the following quantitative data, we compare the two particle group case to the negative A_g large $\tau_{V/T}$ case from section VII and the dusty gas approximation from section IV C. Figure 40 shows the gas mixing width and the S2 particle mixing width. The temporary negative A_{pg} felt at early times causes the gas mixing width to approach zero as it inverts and then begins to grow again. While it remains small at late times, the gas mixing is still significant and on the order of 50% of the dusty gas case. The particle mixing width for S2 particles is large and similar to the negative A_g large $\tau_{V/T}$ case. Overall, the two particle group case behaves similar to the negative A_g large $\tau_{V/T}$ case in mixing width.

Figure 41 shows that the circulation is similar to the negative A_g large $\tau_{V/T}$ case but

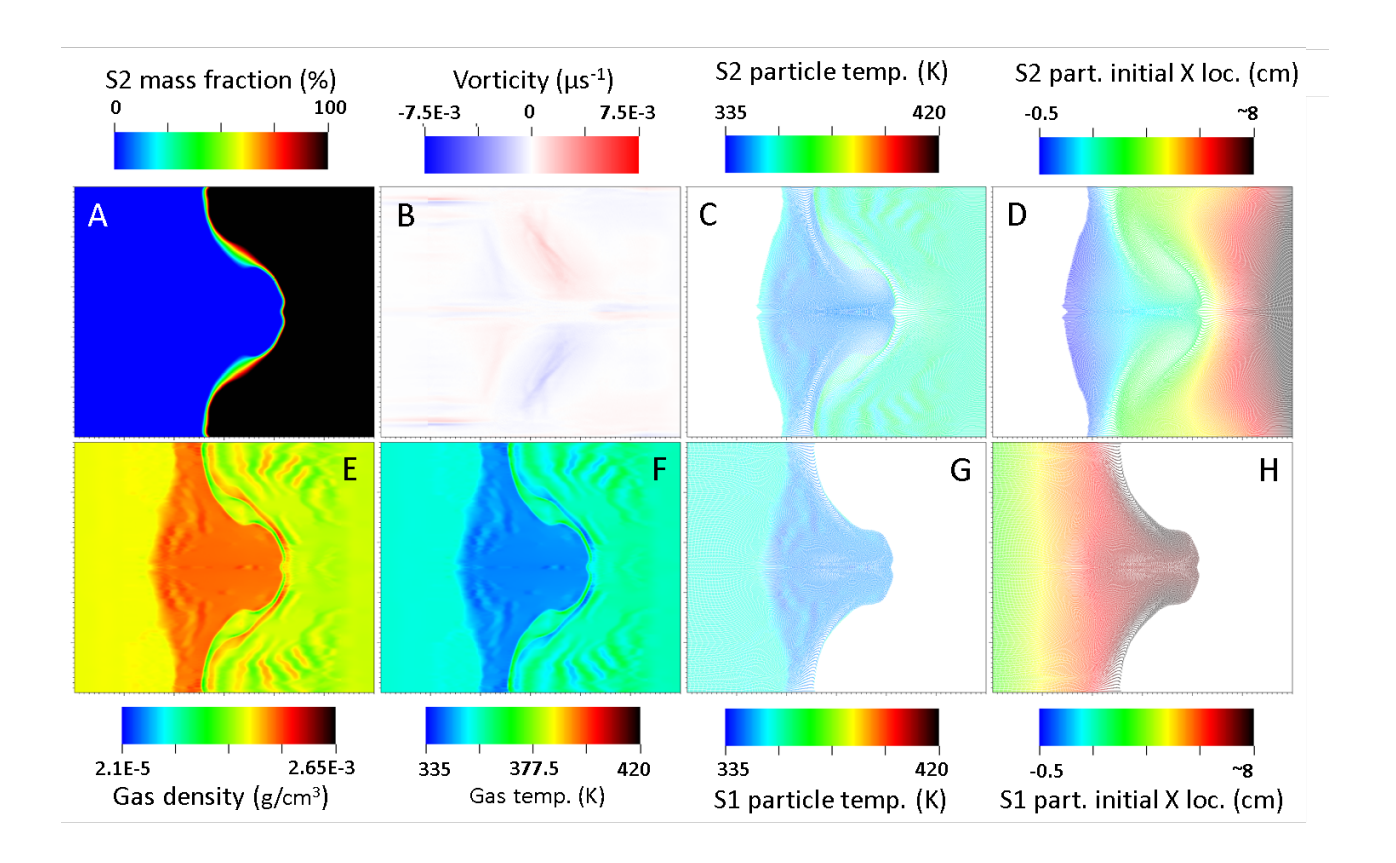


Figure 38. Pseudocolor plots of variable fields at $\tau=200$. A: S2 mass fraction. B: Vorticity. C: S2 particle group temperatures. D: S2 particle group initial X locations. E: Gas density. F: Gas temperature. G: S1 particle group temperatures. H: S1 particle group initial X locations. Note: the X location color bars were scaled so that they extend to $\approx \pm 8$ cm from the interface center.

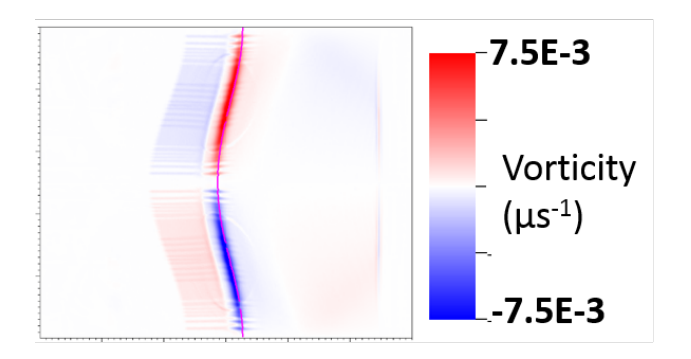


Figure 39. Vorticity deposited on the interface at $\tau \approx 5$ for the two particle group case. The S2 50% mass fraction contour is shown as a line to highlight the interface position.

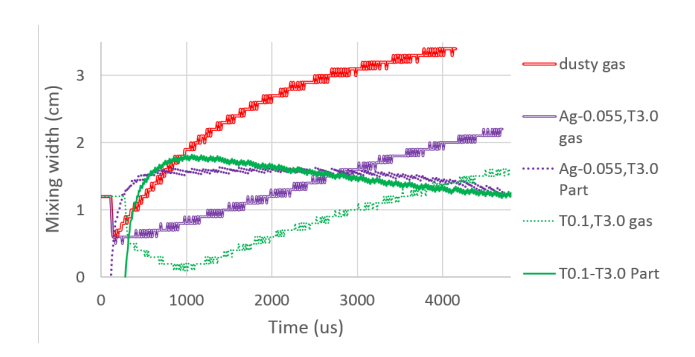


Figure 40. Gas and particle mixing width over time for the two particle group case, the negative A_g and large $\tau_{V/T}$ case and the dusty gas approximation case.

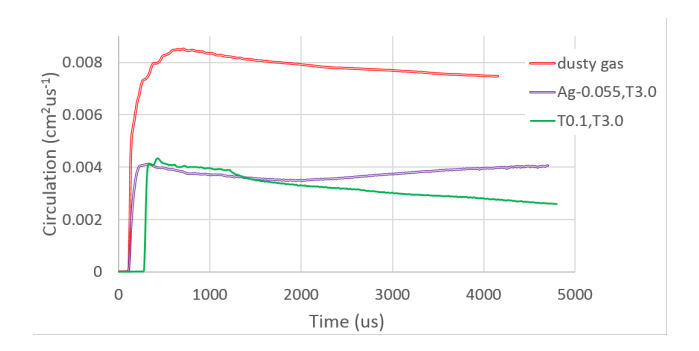


Figure 41. Circulation over time for the two particle group case, the negative A_g and large $\tau_{V/T}$ case and the dusty gas approximation case.

decreases with time as the early time vortex sheet, created by the temporary negative A_{pg} felt by the interface, is stronger, and competition between the two particle groups' vortex layers persists with time. While the circulation is much lower than the dusty gas case, it is still significant considering there is no density difference between the gas or particle-gas systems. The mixed mass plot (fig. 42) shows that the gas mixed mass is lower than any other case and that the S2 particle mixed mass is much larger. The particle mixed mass, though, is still much lower than the negative A_g and long $\tau_{V/T}$ case. It should be noted that the S1 particle mixed mass is or is near zero at all times since the particle lag effects drag the particles deeper into S1. Overall, we can see that the instability created by two particle fields with different relaxation times is smaller than the previous instabilities considered but is still capable of generating circulation and perturbation growth on the order of 50% of the dusty gas case (pure RM instability).

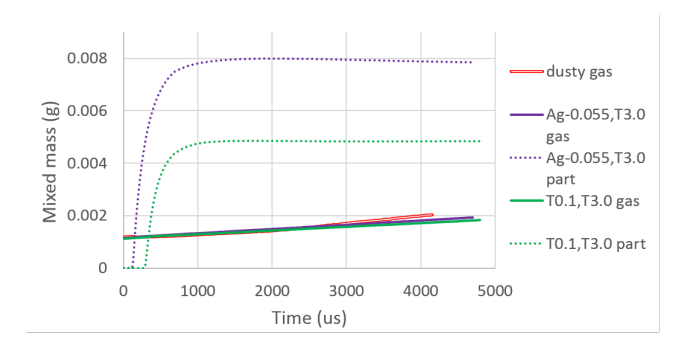


Figure 42. Gas and particle mixed mass over time for the two particle group case, the negative A_g and large $\tau_{V/T}$ case and the dusty gas approximation case.

IX. CONCLUSIONS

The results presented in this computational study have shown only a small sample of the parameters which can be studied and the effects which can be observed in the shock driven multiphase particle-gas instability, but the results have highlighted the broad parameter space and depth of this problem. This work explored the effect of four major parameters which are important to this instability: incident shock Mach number, gas Atwood number, particle-gas Atwood number, and particle relaxation time ratios. The major findings of this work are summarized below for convenience.

For multiphase particle-gas shock driven hydrodynamics with particle mass loading on the order of 25% and particle volume fractions approaching zero, the effects of two-way coupling cannot be ignored. Two-way energy coupling allows the particles to significantly cool the gas and increase its density. This leads to additional baroclinic vorticity deposition and decreased particle temperatures. Two-way momentum coupling is the primary means by which the vortices and instability develop, and without two-way coupling, no instability develops. Even with small particle volumes (less than 0.1%), particle volume terms, which result in drag heating, are important to the temperature distribution of the particles and gas. Without drag heating, the maximum particle temperatures are reduced which would lead to significant errors in predicting particle evaporation or melting.

Even at low particle relaxation times, on the order of 10% of the shock-interface transit time, particle relaxation effects can cause diminished vorticity deposition and alter the hydrodynamics of the interface compared to the dusty gas approximation. At relaxation times on the order of 1% of the shock-interface transit time, the particle relaxation effects become

negligible, and the initial vorticity deposition is the same as the dusty gas approximation. Particle drag heating causes an increased dissipation of circulation after the initial deposition. This could result in a damping of turbulence at later times and should be examined in future 3D simulations.

At higher Mach numbers, particle relaxation effects have a diminished effect on the initial baroclinic vorticity deposition. Baroclinic vorticity deposition is driven by both the pressure gradient of the shock front and the effective density gradient created by the gas and particle field. As Mach number is increased, the pressure gradient becomes more dominant and the particle relaxation effects are weakened. While the hydrodynamics are less sensitive to particle relaxation times at higher Mach numbers, the particle temperatures are more sensitive and show a greater departure from estimations that could be made using the dusty gas approximation. This effect is important to consider in astrophysics regimes where dust processing by strong shocks is studied.

As particle relaxation times increase to be on the order of the shock-interface transit time, particle lag effects completely damp the development of classical Richmyer-Meshkov instability vortices. For large particles, the particle vorticity source term advects relative to the flow creating a diffuse vorticity field and depositing competing vorticity. This reduces the circulation and mixing which takes place between the gas species at the interface but results in a large amount of particle mass being transferred across the interface. This suggests that at late times, turbulent mixing will be diminished, but in high energy applications where phase change will take place, the particle mass will be free to diffuse into the gas carrier phase resulting in additional mixing. At early times, this would result in an increased mixed mass compared to the single phase equivalent, dusty gas, RM instability, but at late times the turbulence damping may be sufficient to reduce the overall mixing. This question should be explored in future work.

At low relaxation times (small particles), the hydrodynamics are dominated by the particle-gas Atwood number. Low gas Atwood numbers with high particle-gas Atwood numbers can generate significant hydrodynamic growth similar to a pure gas instability with an equivalent large gas Atwood number. At high relaxation times (large particles), the gas Atwood number dominates at early times before the particles can equilibriate with the gas. The gas and particle-gas Atwood numbers can be set such that vorticity is imparted by the gas Atwood number effects at early times that is opposite in sign to that which is

deposited by particle-gas Atwood number at later times. This can create two vortex sheets near the interface that are opposite in sign and compete over time to reduce mixing and growth of the interface.

A shock driven particle-gas instability may be created with no gas or particle-gas Atwood number by a difference in particle relaxation times when particles are present in each species. The difference in relaxation time creates a momentary effective particle-gas Atwood number as one particle group reacts before the other, creating an effective density difference for a finite time. For particle groups with relaxation times which differed by an order of magnitude (approximately 10% and 300% of the shock-interface transit time), circulation deposition is significant and is comparable to low particle-gas Atwood number simulations ($A_{pg} \approx -0.055$). This could be an important effect to consider in astrophysical regimes where particle properties may not be uniformly distributed in particle fields which are subjected to shock accelerations.

Many parameters of this instability were left unstudied in this work such as the effect of multiple accelerations like those that occur in the reshock process, and the effect of negative particle-gas Atwood numbers and multiple particle relaxation times created by the presence of multiple particle sizes in the same region. These additional parameters present some exciting possibilities such as the ability to minimize particle and gas mixing through a reshock process. Through reshock, a more turbulent flow can develop which would allow us to study the effect of particle damping on turbulent mixing in 3D simulations. In addition to these parameters which can be studied in the near future, the effect of particle phase change and the associated relaxation time has yet to be studied. The phase change relaxation time may introduce a new variable that allows the particles to have a finite life time during which they can effect the flow. We hope in future work to study these parameters in 2D and 3D simulations and to develop an experimental facility for validation of the results we have shown here.

ACKNOWLEDGMENTS

The authors would like to thank the University of Missouri Research Board for their support of this work. The simulation images in this paper were created using the program VisIt⁵⁵ and the authors would like to thank the VisIt developers for their support of this

program. This work was performed under the auspices of the U.S. Department of Energy by Lawrence Livermore National Laboratory under Contract No.DE-AC52-07NA27344.

REFERENCES

- ¹R. D. Richtmyer, "Taylor instability in shock acceleration of compressible fluids," Communications on Pure and Applied Mathematics **13**, 297–319 (1960).
- ²E. E. Meshkov, "Instability of the interface of two gases accelerated by a shock wave," Fluid Dynamics 4, 101–104 (1972).
- ³V. Smalyuk, D. Casey, D. Clark, M. Edwards, S. Haan, A. Hamza, D. Hoover, W. Hsing, O. Hurricane, J. Kilkenny, J. Kroll, O. Landen, A. Moore, A. Nikroo, L. Peterson, K. Raman, B. Remington, H. Robey, S. Weber, and K. Widmann, "First Measurements of Hydrodynamic Instability Growth in Indirectly Driven Implosions at Ignition-Relevant Conditions on the National Ignition Facility," Physical Review Letters 112, 185003 (2014).
- ⁴J. Kane, R. P. Drake, and B. A. Remington, "An evaluation of the Richtmyer-Meshkov instability in supernova remnant formation," The Astrophysical Journal **511**, 335–340 (1999).
- ⁵A. R. Miles, B. Blue, M. J. Edwards, J. A. Greenough, J. F. Hansen, H. F. Robey, R. P. Drake, C. Kuranz, and D. R. Leibrandt, "Transition to turbulence and effect of initial conditions on three-dimensional compressible mixing in planar blast-wave-driven systems," Physics of Plasmas 12, 056317 (2005).
- $^6\mathrm{I.}$ Cherchneff, "Dust production in Supernovae," arXiv preprint arXiv:1405.1216 (2014).
- ⁷M. Bocchio, A. P. Jones, and J. D. Slavin, "A re-evaluation of dust processing in supernova shock waves." Astronomy & Astrophysics **570**, A32 (2014).
- ⁸D. W. Silvia, B. D. Smith, and J. M. Shull, "NUMERICAL SIMULATIONS OF SU-PERNOVA DUST DESTRUCTION. II. METAL-ENRICHED EJECTA KNOTS," The Astrophysical Journal **748**, 12 (2012).
- ⁹A. K. Speck, A. B. Corman, K. Wakeman, C. H. Wheeler, and G. Thompson, "Silicon Carbide Absorption Features: Dust Formation In The Outflows of Extreme Carbon Stars," The Astrophysical Journal **691**, 1202–1221 (2009).
- ¹⁰P. Woitke, "2d models for dust-driven AGB star winds," Astronomy and Astrophysics **452**, 537–549 (2006).

- ¹¹B. J. Balakumar, G. C. Orlicz, J. R. Ristorcelli, S. Balasubramanian, K. P. Prestridge, and C. D. Tomkins, "Turbulent mixing in a RichtmyerMeshkov fluid layer after reshock: velocity and density statistics," Journal of Fluid Mechanics 696, 67–93 (2012).
- ¹²J. W. Jacobs, V. V. Krivets, V. Tsiklashvili, and O. A. Likhachev, "Experiments on the RichtmyerMeshkov instability with an imposed, random initial perturbation," Shock Waves 23, 407–413 (2013).
- ¹³N. Haehn, C. Weber, J. Oakley, M. Anderson, D. Ranjan, and R. Bonazza, "Experimental investigation of a twice-shocked spherical gas inhomogeneity with particle image velocimetry," Shock Waves **21**, 225–231 (2011).
- ¹⁴J. McFarland, D. Reilly, S. Creel, C. McDonald, T. Finn, and D. Ranjan, "Experimental investigation of the inclined interface RichtmyerMeshkov instability before and after reshock," Experiments in Fluids 55, 1–14 (2014).
- ¹⁵D. Reilly, J. McFarland, M. Mohaghar, and D. Ranjan, "The effects of initial conditions and circulation deposition on the inclined-interface reshocked richtmyer-meshkov instability," Experiments in Fluids 56, 1–16 (2015).
- ¹⁶M. J. Murphy and R. J. Adrian, "PIV space-time resolution of flow behind blast waves," Experiments in Fluids **49**, 193–202 (2010).
- ¹⁷C. Devals, G. Jourdan, J.-L. Estivalezes, E. Meshkov, and L. Houas, "Shock tube spherical particle accelerating study for drag coefficient determination," Shock waves **12**, 325–331 (2003).
- ¹⁸H. Tanno, K. Itoh, T. Saito, A. Abe, and K. Takayama, "Interaction of a shock with a sphere suspended in a vertical shock tube," Shock Waves **13**, 191–200 (2003).
- ¹⁹A. A. Martinez, G. C. Orlicz, and K. P. Prestridge, "A new experiment to measure shocked particle drag using multi-pulse particle image velocimetry and particle tracking," Experiments in Fluids **56** (2015), 10.1007/s00348-014-1854-x.
- ²⁰M. Parmar, A. Haselbacher, and S. Balachandar, "Modeling of the unsteady force for shock–particle interaction," Shock Waves **19**, 317–329 (2009).
- ²¹M. Sun, T. Saito, K. Takayama, and H. Tanno, "Unsteady drag on a sphere by shock wave loading," Shock waves **14**, 3–9 (2005).
- ²²J. L. Wagner, S. J. Beresh, S. P. Kearney, W. M. Trott, J. N. Castaneda, B. O. Pruett, and M. R. Baer, "A multiphase shock tube for shock wave interactions with dense particle fields," Experiments in fluids 52, 1507–1517 (2012).

- ²³P. Vorobieff, M. Anderson, J. Conroy, R. White, C. R. Truman, and S. Kumar, "Vortex Formation in a Shock-Accelerated Gas Induced by Particle Seeding," Physical Review Letters 106, 184503 (2011).
- ²⁴M. Anderson, P. Vorobieff, C. R. Truman, C. Corbin, G. Kuehner, P. Wayne, J. Conroy, R. White, and S. Kumar, "An experimental and numerical study of shock interaction with a gas column seeded with droplets," Shock Waves 25, 107–125 (2015).
- ²⁵S. Balachandar and J. K. Eaton, "Turbulent Dispersed Multiphase Flow," Annual Review of Fluid Mechanics **42**, 111–133 (2010).
- ²⁶F. E. Marble, "Dynamics of dusty gases," Annual Review of Fluid Mechanics 2, 397–446 (1970).
- ²⁷P. Saffman, "On the stability of laminar flow of a dusty gas," Journal of fluid mechanics **13**, 120–128 (1962).
- ²⁸F. H. Harlow, "The particle-in-cell computing method for fluid dynamics," Methods in computational physics **3**, 319–343 (1964).
- ²⁹M. Andrews and P. O'rourke, "The multiphase particle-in-cell (mp-pic) method for dense particulate flows," International Journal of Multiphase Flow **22**, 379–402 (1996).
- ³⁰D. Snider, "An incompressible three-dimensional multiphase particle-in-cell model for dense particle flows," Journal of Computational Physics 170, 523–549 (2001).
- ³¹N. Patankar and D. Joseph, "Modeling and numerical simulation of particulate flows by the eulerian–lagrangian approach," International Journal of Multiphase Flow **27**, 1659–1684 (2001).
- ³²A. A. Amsden, P. O'rourke, and T. Butler, "Kiva-ii: A computer program for chemically reactive flows with sprays," Tech. Rep. (Los Alamos National Lab., NM (USA), 1989).
- ³³L. Torobin and W. Gauvin, "Fundamental aspects of solids-gas flow: Part i: Introductory concepts and idealised sphere motion in viscous regime," The Canadian Journal of Chemical Engineering 37, 129–141 (1959).
- ³⁴L. Cloutman, "A numerical model of particulate transport," Tech. Rep. (Lawrence Livermore National Lab., CA (USA), 1991).
- $^{35}\mathrm{G.}$ Rudinger, Fundamentals of Gas Particle Flow, Vol. 2 (Elsevier, 2012).
- ³⁶C. T. Crowe, J. D. Schwarzkopf, M. Sommerfeld, and Y. Tsuji, Multiphase flows with droplets and particles (CRC press, 2011).
- $^{37}\mathrm{P.}$ ORourke and F. Bracco, "Modelling of drop interactions in thick sprays and a compari-

- son with experiments," Proceedings of the Institution of Mechanical Engineers 9, 101–106 (1980).
- ³⁸R. Di Felice, "The voidage function for fluid-particle interaction systems," International Journal of Multiphase Flow **20**, 153–159 (1994).
- ³⁹G. Rudinger, "Effective drag coefficient for gas-particle flow in shock tubes," Journal of Fluids Engineering **92**, 165–172 (1970).
- ⁴⁰M. L. Wilkins, "Calculation of Elastic Plastic Flow," Tech. Rep. UCRL-7322 (University of California Lawrence Radiation Labratory, 1963).
- ⁴¹T. V. Kolev and R. N. Rieben, "A tensor artificial viscosity using a finite element approach," Journal of Computational Physics **228**, 8336–8366 (2009).
- ⁴²R. W. Sharp and R. T. Barton, "HEMP Advection Model," Tech. Rep. UCID-17809 (Lawrence Livermore Laboratory, 1981).
- ⁴³M. J. Berger and J. Oliger, "Adaptive mesh refinement for hyperbolic partial differential equations," Journal of computational Physics **53**, 484–512 (1984).
- ⁴⁴M. J. Berger and P. Colella, "Local adaptive mesh refinement for shock hydrodynamics," Journal of computational Physics **82**, 64–84 (1989).
- ⁴⁵J. A. McFarland, D. Reilly, W. Black, J. A. Greenough, and D. Ranjan, "Modal interactions between a large-wavelength inclined interface and small-wavelength multimode perturbations in a richtmyer-meshkov instability," Physical Review E **92**, 013023 (2015).
- ⁴⁶B. Morgan and J. Greenough, "Large-eddy and unsteady rans simulations of a shock-accelerated heavy gas cylinder," Shock Waves , 1–29 (2015).
- ⁴⁷B. J. Olson and J. Greenough, "Large eddy simulation requirements for the Richtmyer-Meshkov instability," Physics of Fluids **26**, 044103 (2014).
- ⁴⁸W. Ranz and W. Marshall, "Evaporation from drops," Chemical Engineering Progress **48**, 141–146 (1952).
- ⁴⁹B. D. Collins and J. W. Jacobs, "PLIF flow visualization and measurements of the Richt-myerMeshkov instability of an air/SF6 interface," Journal of Fluid Mechanics **464**, 113–136 (2002).
- ⁵⁰G. Peng, N. J. Zabusky, and S. Zhang, "Vortex-accelerated secondary baroclinic vorticity deposition and late-intermediate time dynamics of a two-dimensional RichtmyerMeshkov interface," Physics of Fluids **15**, 3730 (2003).
- 51 L. D. Cloutman, "Analytical solutions for the trajectories and thermal histories of unforced

- particulates," American Journal of Physics 56, 643-645 (1988).
- ⁵²M. Stanic, J. McFarland, R. F. Stellingwerf, J. T. Cassibry, D. Ranjan, R. Bonazza, J. A. Greenough, and S. I. Abarzhi, "Non-uniform volumetric structures in Richtmyer-Meshkov flows," Physics of Fluids 25, 106107 (2013).
- ⁵³B. Motl, J. Oakley, D. Ranjan, C. Weber, M. Anderson, and R. Bonazza, "Experimental validation of a RichtmyerMeshkov scaling law over large density ratio and shock strength ranges," Physics of Fluids **21**, 126102 (2009).
- ⁵⁴A. Ahmed and S. Elghobashi, "On the mechanisms of modifying the structure of turbulent homogeneous shear flows by dispersed particles," Physics of Fluids (1994-present) **12**, 2906–2930 (2000).
- ⁵⁵H. Childs, E. Brugger, B. Whitlock, J. Meredith, S. Ahern, D. Pugmire, K. Biagas, M. Miller, C. Harrison, G. H. Weber, H. Krishnan, T. Fogal, A. Sanderson, C. Garth, E. W. Bethel, D. Camp, O. Rübel, M. Durant, J. M. Favre, and P. Navrátil, "VisIt: An End-User Tool For Visualizing and Analyzing Very Large Data," in *High Performance Visualization–Enabling Extreme-Scale Scientific Insight*, Vol. 1 (Taylor and Francis, Boca Raton, 2012) Chap. 16, pp. 357–372.